The Pristine survey – XV. A CFHT ESPaDOnS view on the Milky Way halo and disc populations

R Lucchesi, C Lardo, P Jablonka, F Sestito, L Mashonkina, A Arentsen, W Suter, K Venn, N Martin, E Starkenburg, et al.

Monthly Notices of the ROYAL ASTRONOMICAL SOCIETY

MNRAS **511,** 1004–1021 (2022) https://doi.org/10.1093/mnras/stab3721
Advance Access publication 2022 January 06

The Pristine survey – XV. A CFHT ESPaDOnS view on the Milky Way halo and disc populations

R. Lucchesi [1,2★] C. Lardo [1,3] P. Jablonka,[1,4] F. Sestito [5] L. Mashonkina [6] A. Arentsen [7] W. Suter,[1] K. Venn [5] N. Martin [7,8] E. Starkenburg,[9] D. Aguado [10] V. Hill,[11] G. Kordopatis,[11] J. F. Navarro,[5] J. I. González Hernández,[12,13] K. Malhan[14] and Z. Yuan[7]

[1]*Institut de Physique, Laboratoire d'astrophysique, École Polytechnique Fédérale de Lausanne (EPFL), Observatoire, CH-1290 Versoix, Switzerland*
[2]*European Southern Observatory, Karl-Schwarzschild-str 2, D-85748 Garching bei München, Germany*
[3]*Dipartimento di Fisica e Astronomia, Università degli Studi di Bologna, Via Gobetti 93/2, I-40129 Bologna, Italy*
[4]*GEPI, Observatoire de Paris, Université PSL, CNRS, 5 Place Jules Janssen, F-92190 Meudon, France*
[5]*Department of Physics and Astronomy, University of Victoria, PO Box 3055, STN CSC, Victoria, BC V8W 3P6, Canada*
[6]*Institute of Astronomy of the Russian Academy of Sciences, Pyatnitskaya st. 48, 119017 Moscow, Russia*
[7]*Université de Strasbourg, CNRS, Observatoire astronomique de Strasbourg, UMR 7550, F-67000 Strasbourg, France*
[8]*Max-Planck-Institut für Astronomie, Königstuhl 17, D-69117 Heidelberg, Germany*
[9]*Kapteyn Astronomical Institute, University of Groningen, Postbus 800, NL-9700 AV Groningen, the Netherlands*
[10]*Institute of Astronomy, University of Cambridge, Madingley Road, Cambridge CB3 0HA, UK*
[11]*Université Côte d'Azur, Observatoire de la Côte d'Azur, CNRS, Laboratoire Lagrange, F-06300 Nice, France*
[12]*Instituto de Astrofísica de Canarias, Vía Lactea, E-38205 La Laguna, Tenerife, Spain*
[13]*Departamento de Astrofísica, Universidad de La Laguna, E-38206 La Laguna, Tenerife, Spain*
[14]*The Oskar Klein Centre for Cosmoparticle Physics, Department of Physics, Stockholm University, AlbaNova, SE-10691 Stockholm, Sweden*

Accepted 2021 December 17. Received 2021 December 8; in original form 2021 June 24

ABSTRACT

We present a one-dimensional, local thermodynamic equilibrium homogeneous analysis of 132 stars observed at high resolution with ESPaDOnS. This represents the largest sample observed at high resolution ($R \sim 40\,000$) from the *Pristine* survey. This sample is based on the first version of the *Pristine* catalogue and covers the full range of metallicities from [Fe/H] ~ -3 to $\sim +0.25$, with nearly half of our sample (58 stars) composed of very metal-poor (VMP) stars ([Fe/H] ≤ -2). This wide range of metallicities provides the opportunity of a new detailed study of the Milky Way stellar population. Because it includes both dwarf and giant stars, it also enables the analysis of any potential bias induced by the *Pristine* selection process. Based on *Gaia* EDR3, the orbital analysis of this *Pristine*-ESPaDOnS sample shows that it is composed of 65 halo stars and 67 disc stars. After a general assessment of the sample chemical properties with the α-elements Mg and Ca, we focus on the abundance of carbon and the neutron capture elements Ba and Sr. While most of our VMP subsample is carbon normal, we also find that 14 stars out of the 38 stars with [Fe/H] ≤ -2 and measured carbon abundances turn out to be carbon-enhanced metal-poor (CEMP) stars. We show that these CEMP stars are nearly exclusively (i.e. 12 stars out of 14) in the regime of low luminosity, unevolved, dwarf stars, which we interpret as the consequence of bias of the *Pristine* filter against C-rich giants. Among the VMP stars, we identify two CEMP stars with no enhancement in neutron-capture process elements and another one enriched in s-process element. Finally, one VMP star is found with a very low [Sr/Fe] abundance ratio for its metallicity, as expected if it had been accreted from an ultra-faint dwarf galaxy.

Key words: stars: abundances – galaxies: dwarf – galaxies: formation – Local Group.

1 INTRODUCTION

The most metal-poor stars in the Galaxy and its close satellites are witnesses of the early stages of star formation in the Universe (e.g. Pagel 1997; Bromm & Larson 2004; Heger & Woosley 2010; Frebel & Norris 2015, and references therein). Their formation follows the explosions of a few population III (Pop III) supernovae only. Hence, their elemental abundances reflect the physical conditions and the nucleosynthesis of the primordial chemical evolution (e.g. Beers, Preston & Shectman 1992; Cayrel et al. 2004; Beers & Christlieb 2005; Keller et al. 2007; Christlieb et al. 2008; Caffau et al. 2013; Yong et al. 2013; Roederer et al. 2014; Jacobson et al. 2015; Frebel 2018).

The detection of very metal-poor (VMP; [Fe/H] ≤ -2.0), extremely metal-poor (EMP; [Fe/H] ≤ -3.0), and ultra metal-poor (UMP; [Fe/H] ≤ -4.0) stars is a challenging task that requires surveying large volumes of the sky.[1] Indeed, many observational efforts have been devoted to the search and identification of such key stellar

★ E-mail: romain.lucchesi@epfl.ch (RL)

[1]In a high Galactic latitude field towards the anticentre direction only $\sim$1/2000 stars in the magnitude range between $14 < V < 18$ are expected to have metallicity less than [Fe/H] ≤ -3; (Youakim et al. 2017).

population – e.g. the HK objective-prism survey (Beers et al. 1992); the RAdial Velocity Experiment survey (Steinmetz et al. 2006); the Hamburg/ESO objective-prism survey (Christlieb et al. 2008); the Sloan Extension for Galactic Understanding and Exploration Survey (Yanny et al. 2009); the LAMOST Experiment for Galactic Understanding and Exploration (Deng et al. 2012); the Apache Point Observatory Galactic Evolution Experiment (Majewski, APOGEE Team & APOGEE-2 Team 2016); and the SkyMapper Southern Sky Survey (Keller et al. 2007).

Along these lines, *Pristine* is a photometric survey designed to efficiently pre-select VMP star candidates (Starkenburg et al. 2017; Youakim et al. 2017; Aguado et al. 2019). It takes advantage of a narrow-band filter centred on the Ca H&K spectral lines and of the large field of view of MegaCam at the Canada–France–Hawaii Telescope (CFHT). Briefly, the *Pristine* selection method combines information from the metallicity-sensitive Ca H&K filter with broad-band photometry from large-field, multiband photometric surveys; e.g. the Sloan Digital Survey (SDSS; York et al. 2000; Eisenstein et al. 2011; Blanton et al. 2017) and *Gaia* DR2 (Gaia Collaboration 2016, 2018).

Spectroscopic follow-up of EMP star candidates is ongoing. These observations are conducted both at medium and high spectroscopic resolution (Caffau et al. 2017; Youakim et al. 2017; Starkenburg et al. 2018; Aguado et al. 2019; Bonifacio et al. 2019; Caffau et al. 2020; Venn et al. 2020; Kielty et al. 2021). The detailed chemical analysis of individual stars allows us to address three main threads of open issues related to stellar evolution and galaxy formation: (i) the nature and properties of the first stars, (ii) how and when the different components of the structure of the Milky Way (MW) assemble, and, finally, (iii) in the hierarchical galaxy formation paradigm, the mass and the degree of chemical evolution of the dwarf galaxy building blocks.

The existence of α-poor stars ([(Mg+Ca)/Fe] $\leq$ 0) in some of the *Pristine* subsample was reported by Caffau et al. (2020) in their ESO/FORS2 medium-resolution spectroscopic follow-up. These stars were found in a metallicity regime that is more metal-poor ([Fe/H] < -1.2) than the sample of Nissen & Schuster (2010), which is interpreted as the result of quiescent star formation forming the MW thin disc (Khoperskov et al. 2021). Such metal deficient and α-poor stars were also identified in other studies (e.g. Ivans et al. 2003; Cohen et al. 2013). Their origin is still unclear and could be heterogeneous, such as a formation from pockets of interstellar medium enhanced in Type Ia supernovae (SNeIa) products, biased initial mass function (IMF) sampling, or accretion of merging dwarf systems (Sakari et al. 2019; Xing et al. 2019). The present *Pristine* sample is large enough to shed some light on the fraction of α-poor stars in the MW halo.

Carbon-enhanced metal-poor (CEMP; i.e. stars having [C/Fe] $\geq$ 1.0 according to the definition given in Beers & Christlieb 2005) represent an increased fraction of the halo component of the MW with decreasing metallicity (see Frebel & Norris 2015, for a complete discussion). For three metallicity bins in the range between –4.5 < [Fe/H] < -3.0, Yong et al. (2013) found that the fraction of CEMP stars was increasing from 0.22 to 0.32, and 0.33 with decreasing metallicity, up to 1.00 for [Fe/H] < -4.5. Higher fractions were derived by Placco et al. (2014) when correcting for internal mixing effects depleting surface carbon abundance with stellar evolution – e.g. they derive a fraction of 0.43, 0.60, 0.70, and 1.00, respectively, for the same metallicity bins defined in Yong et al. (2013). The exact origin of this increase in CEMP stars towards lower metallicities has yet to be unveiled, however, this result suggest that significant amounts of carbon were produced in the early Universe. This production could be a necessary condition for the transition from massive pop III to low-mass stars (Bromm & Loeb 2003). However, the discoveries of SDSS J102915+172927 at [Fe/H] $= -4.73$ (Caffau et al. 2011) and Pristine 221.8781+9.7844 at -4.66 (Starkenburg et al. 2018), two stars with a significant low enrichment of carbon, nitrogen, and oxygen suggest that there must have been more than one formation channel of low-mass stars in the early Universe. Unexpectedly *Pristine* has found two contradictory results on this matter. While Aguado et al. (2019) reported a normal fraction of CEMP stars, Caffau et al. (2020) found a fraction of CEMP stars much lower than those provided by Placco et al. (2014), thereby suggesting some sensitivity of the *Pristine* filter to carbon abundance. This issue can be addressed in this study.

In the following, we present the analysis of the 132 bright ($V < 15.5$) metal-poor candidates from the original 1000 deg^2 of the *Pristine* survey, calibrated using the original SDSS gri photometry and observed at the CFHT with the high-resolution spectrograph ESPaDOnS. Out of this full sample, Venn et al. (2020) presented the detailed abundances of 10 elements (Na, Mg, Ca, Sc, Ti, Cr, Fe, Ni, Y, and Ba) for the 28 VMP stars identified at the time, as well as the analysis of their orbital properties. Because the full sample comes from the first stages of the *Pristine* calibration, the confirmation of very metal-deficient stars does not reach a success rate as high as in the later stages. Nevertheless, near half of the present sample (58 stars) is composed of VMP stars ([Fe/H] ≤ -2). The more metal-rich stars offer us the opportunity of a new and detailed study of the MW halo stellar population.

This paper is organized as follows: in Section 2, we first discuss observations and data reduction. The abundance analysis is presented in Section 3 and the discussion of the abundances of C, Mg, Ca, Sr, and Ba takes place in Section 4. In Section Section 5, we look into the orbits of our sample stars. Finally, Section 6 summarizes our results and conclusions.

2 OBSERVATIONAL MATERIAL

2.1 Source catalogue and sample selection

The targets were selected from the *Pristine* diagnostics originally presented in Starkenburg et al. (2017). Stars were selected upon their probability to be VMP, in the bright ($V \lesssim 15.5$) regime of the original $\sim$1000 deg^2 footprint of *Pristine*.

The final sample consists in 132 stars and includes the following:

(i) 112 stars which were introduced in Venn et al. (2020). [Fe/H] was spectroscopically derived only for a subset of those (86) using the equivalent widths (EWs) of six selected iron lines (four Fe I lines and two Fe II lines). In the following, we adopt the same nomenclature as Venn et al. (2020) and refer to this metallicity estimate as the quick six (Q6) one. Only stars with metallicity estimate [Fe/H] ≤ -2.5 were then retained for further spectroscopic chemical analysis (28 stars).

(ii) 20 new stars from the CFHT ESPaDOnS programs 16BF10, 17AF09, and 17BF18.

Fig. 1 shows the distribution of the full sample in the dereddened g_0 SDSS magnitude, with $E(B-V)$ values taken from the galactic reddening maps of Schlegel, Finkbeiner & Davis (1998). Stellar magnitudes range from $g_0 = 13.6$ to 15.3 with a peak around $g_0 = 14.7$. Table 1 provides the coordinates, dereddened g_0 and i_0 SDSS magnitudes along with the corresponding $E(B-V)$ values, and dereddened *Pristine* CaH&K magnitudes for all stars analysed in this study.

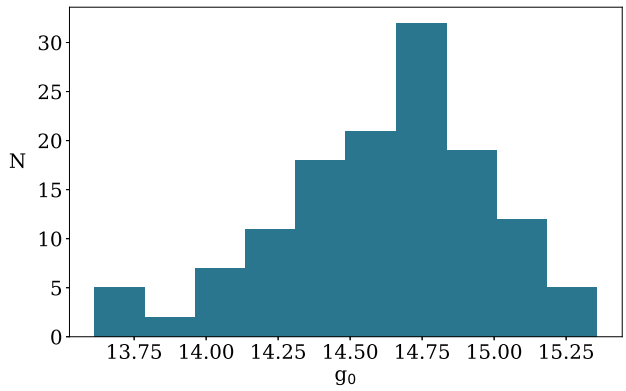

Figure 1. Histogram of the SDSS dereddened g magnitudes (g_0) of the 132 stars analysed in this work.

The full data set is analysed in a homogeneous way. The data reduction has been improved compared to Venn et al. (2020); all stellar atmospheric parameters are now spectroscopically derived and we provide detailed chemical abundances for C, Mg, Ca, Fe, Sr, and Ba.

2.2 Observations and data reduction

The observations were performed during the periods 2016A and 2018B with the high-resolution spectrograph ESPaDOnS at the CFHT (Donati et al. 2006). To enable a good sky subtraction, ESPaDOnS was used in the 'star + sky' mode, providing a high-resolution ($R = 68\,000$) spectrum from 4000 to 10 000 Å. Exposure times range from ∼12 min for the brightest targets to ∼120 min for the faintest ones.

The data reduction was performed with the dedicated pipeline LIBRE-ESPRIT.[2] This includes bias subtraction, flat fielding, wavelength calibration, and spectral extraction. ESPaDOnS records 40 orders and each of them is curved. LIBRE-ESPRIT proceeds in two steps. First, the pipeline performs a geometrical analysis from a sequence of calibration exposures. The position and shape of each order is derived from a mean flat-field image. The details of the wavelength-to-pixel relationship along and across each spectral order is measured from a thorium lamp exposure. Second, LIBRE-ESPRIT performs an optimal extraction of each object spectrum, using the geometrical information found in the previous step. It computes the intensity spectra with error bars, and applies corrections to compensate for Earth's motion.

The Echelle orders were merged using a procedure developed by the authors of this paper. In short, the script isolates the different echelle orders to remove, in the overlapping wavelength regions, the part with the lowest signal-to-noise ratio (SNR). The orders are then combined again with a sigma clipping routine.

Spectra with multiple exposures were corrected for radial velocity (RV) shifts before combination. RVs were measured with the DAOSPEC package (Stetson & Pancino 2008) using the 4DAO wrapper (Mucciarelli 2013). The spectra were then degraded to $R = 40\,000$ to increase the SNR and allow for the automatic EW measurement under the assumption that the line profile has a Gaussian shape. The final RV corrected and combined spectra are normalized using DAOSPEC in three wavelength ranges (4000–4800, 4800–5800, and 5800–6800 Å), using a 40–60 order polynomial. The final RV measurements and their associated errors, along with the number of exposures for each stars, are presented in Table 1.

Fig. 2 illustrates how the quality of the reduced spectra is improved by this procedure. It shows a portion of the original ESPaDOnS spectrum of the star Pr_236.1077+10.5311 and its spectrum after our optimal merging procedure, degraded to a resolution of $R = 40\,000$.

3 ATMOSPHERIC PARAMETERS AND CHEMICAL ABUNDANCES

The chemical abundances of iron, carbon, the α- Mg and Ca, and neutron (n)-capture (Sr and Ba) elements are calculated in 1D local thermodynamic equilibrium (LTE) with TURBOSPECTRUM (Plez 2012) combined with MARCS model atmospheres.[3]

The EWs of unblended spectral lines with Gaussian shape together with their associated uncertainties were measured with DAOSPEC (Stetson & Pancino 2008) that was launched iteratively with the code 4DAO (Mucciarelli 2013).

A χ^2 minimization between the observed and synthetic spectra was applied for the strong and blended lines, and for the elements presenting hyper fine splitting (HFS) of their energy levels such as barium and carbon. The latter was estimated from the CH molecular feature at 4300 Å. All synthetic spectra were convoluted to the instrumental resolution, then rebinned at the same pixel step as the observed spectra.

The abundance analysis is carried out with our own code. It enables the interpolation of the stellar atmosphere models, allows the derivations of the atmospheric parameters and chemical abundances from EW measurements, as well as enables a spectral synthesis χ^2 minimization for a set of chosen lines and elements. Spectral synthesis is typically done over small wavelength ranges, centred on the line of interest. The abundance of an element X is varied between $-2.0 \leq$ [X/Fe] $\leq +2.0$ dex in steps of 0.1 dex, and refined in a second iteration with smaller steps.

The linelist used in the calculations is the same as in Lucchesi et al. (2020). It combines the list from Jablonka et al. (2015), Tafelmeyer et al. (2010), and Van der Swaelmen et al. (2013). The data for the selected atomic and molecular transitions are taken from the VALD data base (Piskunov et al. 1995; Ryabchikova et al. 1997; Kupka et al. 2000). The solar abundances are taken from Asplund et al. (2009).

3.1 Atmospheric parameters and metallicities

The stellar atmospheric parameters, i.e. effective temperature ($T_{\rm eff}$), surface gravity ($\log g$), micro-turbulence velocity ($v_{\rm t}$), and metallicity ([Fe/H]), were adjusted spectroscopically using the classical EW method. Only Fe lines with EW $\geq$ 25 mÅ were considered, in order to exclude the weak and noisy ones. Lines with EW $\geq$ 110 mÅ were also excluded from the EW analysis, in order to avoid the flat part of the curve of growth that is less sensitive to the abundance. These lines are highly sensitive to the microturbulent velocity and the velocity fields. Moreover the Gaussian approximation of the line profile starts to fail. Lines with excitation potential $\chi_{\rm ex} > 1.4$ eV were also rejected in order to minimize non-local thermodynamic equilibrium (NLTE) effects. Finally, the Fe I lines at wavelength shorter than $\lambda \leq 4500$ Å

[2] https://www.cfht.hawaii.edu/Instruments/Spectroscopy/Espadons/Espadons_esprit.html

[3] https://marcs.astro.uu.se/

Table 1. Right ascension, declination, dereddened SDDS g and i magnitudes, averaged radial velocities, uncertainties on radial velocities, spectroscopic $T_{\rm eff}$ log g micro-turbulence velocities and metallicities for the 132 stars analysed. Stars marked with * were rejected by the new *Pristine* photometric selection. Stars marked with † are three fast rotators and discarded from the analysis.

Star	RA (deg)	Dec. (deg)	g_0	i_0	CaHK$_0$	$E(B-V)$	RV (km s^{-1})	$\sigma_{\rm RV}$	$T_{\rm eff}$ (K)	log g (cgs)	$v_{\rm t}$ (km s^{-1})	[Fe/H] (dex)
Pr_134.3232+17.6970	134.3232	17.6970	14.671	14.310	15.002	0.033	+115.27 (5)	1.78	6350	4.40	1.12	− 2.63
Pr_180.0090+3.7165	182.5090	03.7165	13.613	13.040	14.227	0.018	− 17.30 (1)	1.32	5200	4.40	1.12	− 0.18*
Pr_180.2206+9.5683	180.2206	09.5683	15.186	14.370	15.890	0.020	+22.12 (6)	0.46	5050	1.86	1.55	− 2.96
Pr_180.3790+0.9470	180.3790	00.9470	14.353	13.776	14.987	0.019	− 57.47 (1)	0.90	5684	3.70	1.05	− 0.74
Pr_180.7918+3.4084	180.7918	03.4084	13.748	12.456	14.884	0.027	+21.20 (1)	0.81	4800	3.70	1.26	− 0.08*
Pr_180.9118+11.3258	180.9118	11.3258	14.244	13.630	14.855	0.026	+33.98 (1)	0.95	5800	3.80	1.15	− 0.49*
Pr_181.2243+7.4160	181.2243	07.4160	15.057	14.694	15.450	0.014	− 146.70 (2)	0.77	6455	3.81	1.24	− 2.92
Pr_181.3119+11.6850	181.3119	11.6850	14.270	13.488	15.006	0.032	+1.49 (2)	0.02	5300	4.60	1.08	− 1.84*
Pr_181.3473+11.6698	181.3473	11.6698	14.414	13.722	15.006	0.032	+11.90 (2)	0.02	5900	4.45	1.11	− 0.49
Pr_181.3708+11.7636	181.3708	11.7636	14.443	13.689	15.119	0.033	+79.06 (1)	3.03	5494	3.18	1.36	− 1.48†
Pr_181.4395+1.6294	181.4395	01.6294	14.969	14.052	15.795	0.021	+206.58 (1)	2.00	4935	1.80	1.80	− 2.50
Pr_181.6954+13.8076	181.6954	13.8076	14.714	14.055	15.384	0.030	+78.01 (1)	1.06	5608	3.60	1.05	− 0.80
Pr_182.1670+3.4771	182.1670	03.4771	14.209	13.107	14.967	0.020	− 19.09 (1)	0.64	5350	4.45	1.11	− 0.35*
Pr_182.5364+0.9431	182.5364	00.9431	15.053	14.645	15.476	0.029	+222.71 (2)	0.34	6270	3.75	1.25	− 1.74
Pr_182.8521+14.1594	182.8521	14.1594	14.409	13.462	15.333	0.045	+78.56 (1)	1.35	4959	1.75	1.60	− 1.79
Pr_183.6850+4.8619	183.6850	04.8619	15.038	14.718	15.374	0.017	+41.00 (2)	0.30	6491	4.44	1.11	− 3.16
Pr_185.4112+7.4778	185.4112	07.4778	14.847	14.412	15.234	0.020	+175.18 (2)	0.40	6304	4.53	1.09	− 1.85*
Pr_187.8517+13.4560	187.8517	13.4560	13.914	13.382	14.269	0.025	+1.99 (1)	0.43	5700	4.10	1.18	− 0.45*
Pr_187.9786+8.7294	187.9786	08.7294	15.190	14.532	15.775	0.018	− 54.11 (2)	0.06	5618	3.66	1.27	− 0.50
Pr_188.1264+8.7740	188.1264	08.7740	14.528	13.780	15.228	0.017	− 48.83 (1)	1.11	5600	3.60	1.00	− 1.05
Pr_189.9449+11.5535	189.9449	11.5535	14.427	14.033	14.812	0.037	+30.35 (1)	6.00	6491	3.83	1.23	− 2.57
Pr_190.2669+11.1092	190.2669	11.1092	14.076	13.854	14.759	0.027	− 15.71 (1)	1.18	5800	4.20	1.16	− 0.34*
Pr_190.5813+12.8577	190.5813	12.8577	14.327	13.632	14.779	0.030	+4.42 (1)	0.70	5800	4.20	1.16	− 0.20*
Pr_190.6313+8.5138	190.6313	08.5138	15.114	14.511	16.060	0.021	− 64.16 (2)	0.02	5500	3.80	1.24	− 0.24
Pr_192.2121+15.9263	192.2121	15.9263	14.843	13.809	15.837	0.025	− 4.56 (1)	0.76	5600	4.30	1.14	+0.25
Pr_192.4285+15.9119	192.4285	15.9119	14.238	13.795	15.031	0.026	− 62.24 (1)	0.62	5450	4.65	1.07	− 0.49*
Pr_192.8540+15.8199	192.8540	15.8199	14.277	13.748	14.763	0.023	+0.98 (1)	0.39	5700	4.05	1.19	− 0.20*
Pr_192.9068+6.8314	192.9068	06.8314	13.766	13.017	14.490	0.034	+15.64 (1)	1.52	5800	4.25	1.15	− 0.35
Pr_193.1159+8.0557	193.1159	08.0557	14.660	14.224	15.129	0.026	+42.13 (1)	4.43	6100	4.55	1.09	− 1.85
Pr_193.1501+15.7966	193.1501	15.7966	13.757	13.536	14.373	0.025	+9.57 (1)	0.93	5800	4.00	1.20	− 0.31*
Pr_193.5542+11.5036	193.5542	11.5036	14.460	13.681	15.087	0.032	+16.20 (1)	0.66	5679	4.15	1.17	− 0.30
Pr_193.8390+11.4150	193.8390	11.4150	15.072	13.983	16.070	0.030	+2.53 (2)	0.07	4650	1.22	1.76	− 2.91
Pr_196.3755+8.5138	196.3755	08.5138	14.914	14.051	15.656	0.029	− 72.24 (1)	3.59	5012	1.73	1.65	− 2.77
Pr_196.4126+14.3177	196.4126	14.3177	14.884	14.003	15.634	0.029	− 49.36 (2)	0.00	5702	4.55	1.09	− 0.44
Pr_196.5323+8.7716	196.5323	08.7716	14.157	13.874	14.491	0.031	− 100.40 (2)	1.59	6483	4.55	1.09	− 2.55
Pr_196.5453+12.1211	196.5453	12.1211	14.745	14.468	15.090	0.028	+54.47 (2)	0.24	5950	3.40	1.32	− 2.51
Pr_196.6013+15.6768	196.6013	15.6768	14.624	14.001	15.438	0.027	− 103.91 (2)	0.17	5600	4.60	1.08	− 0.69
Pr_197.5045+15.6970	197.5045	15.6970	13.980	13.807	14.490	0.022	− 59.46 (1)	0.98	5920	4.05	1.19	− 0.80*
Pr_197.9861+12.3578	197.9861	12.3578	15.074	14.626	15.647	0.028	+114.83 (2)	0.35	6050	3.80	1.24	− 1.22
Pr_198.5288+12.1493	198.5288	12.1493	14.232	14.111	14.840	0.024	− 26.75 (1)	1.23	6120	4.25	1.15	− 0.59*
Pr_198.5495+11.4125	198.5495	11.4125	14.357	13.988	14.772	0.022	+74.45 (1)	5.31	6494	4.35	1.13	− 2.20
Pr_199.9269+8.3816	199.9269	08.3816	14.100	13.423	15.092	0.022	+3.17 (1)	0.54	5300	4.55	1.09	− 0.15*
Pr_200.0999+13.7229	200.0999	13.7229	15.282	14.223	16.288	0.024	+189.83 (4)	0.56	4750	1.24	1.75	− 2.48
Pr_200.5298+8.9768	200.5298	08.9768	15.358	14.664	16.306	0.027	+96.79 (2)	0.14	5363	3.45	1.20	− 1.02
Pr_200.7620+9.4376	200.7620	09.4376	14.695	14.096	15.680	0.023	+33.26 (1)	0.68	5650	4.35	1.13	− 0.15
Pr_201.1159+15.4382	201.1159	15.4382	14.548	13.859	15.586	0.021	− 5.77 (1)	0.70	5589	4.40	1.12	− 0.19
Pr_202.3435+13.2291	202.3435	13.2291	14.398	13.840	14.795	0.021	+100.81 (2)	0.20	5950	2.80	1.50	− 0.75
Pr_203.2831+13.6326	203.2831	13.6326	15.116	14.249	15.833	0.024	− 139.55 (1)	3.42	5008	1.95	1.45	− 2.70
Pr_204.9008+10.5513	204.9008	10.5513	14.894	14.617	15.171	0.031	− 246.62 (1)	6.02	6718	4.22	1.16	− 2.66
Pr_205.1342+13.8234	205.1342	13.8234	14.803	14.188	15.402	0.022	+126.90 (1)	3.05	5462	2.90	1.42	− 2.12
Pr_205.8132+15.3832	205.8132	15.3832	14.678	14.371	15.076	0.032	+121.42 (1)	5.22	6718	4.23	1.15	− 2.13
Pr_206.3487+9.3099	206.3487	09.3099	14.365	14.027	14.726	0.026	+157.19 (1)	4.17	6522	3.94	1.21	− 1.80
Pr_207.9961+1.1795	207.9961	01.1795	14.306	13.493	14.823	0.030	+36.17 (1)	0.51	5450	4.40	1.12	− 0.49*
Pr_208.0799+4.4267	208.0799	04.4267	14.686	14.132	15.151	0.026	− 129.96 (1)	5.27	5572	2.97	1.41	− 2.77
Pr_209.2123+1.5275	209.2123	01.5275	14.562	14.030	15.100	0.035	+13.53 (1)	2.67	5540	3.30	1.15	− 1.90
Pr_209.7189+10.8613	209.7189	10.8613	14.642	14.250	15.069	0.024	− 136.51 (2)	0.33	6358	4.40	1.12	− 1.98*
Pr_209.9364+15.9251	209.9364	15.9251	14.903	14.611	15.281	0.021	− 91.43 (2)	0.37	6664	3.96	1.21	− 2.25
Pr_210.0175+14.6289	210.0175	14.6289	14.789	14.079	15.464	0.018	− 74.32 (2)	0.67	5150	2.37	1.53	− 2.67
Pr_210.0316+14.0027	210.0322	14.0036	14.590	14.019	15.247	0.016	+22.68 (2)	0.03	5400	3.55	1.29	− 0.98*
Pr_210.7513+12.7744	210.7513	12.7744	14.881	13.714	16.127	0.028	+40.58 (1)	1.65	4652	1.35	1.60	− 2.12
Pr_210.8633+8.1798	210.8633	08.1798	14.675	14.067	15.237	0.024	− 12.33 (3)	0.79	5542	3.31	1.34	− 1.95
Pr_211.2766+10.3280	211.2766	10.3280	14.825	14.393	15.348	0.022	+44.59 (1)	1.79	5740	3.75	1.25	− 1.39*

Table 1 – *continued*

Star	RA (deg)	Dec. (deg)	g_0	i_0	CaHK$_0$	$E(B-V)$	RV (km s^{-1})	σ_{RV}	T_{eff} (K)	log g (cgs)	v_t (km s^{-1})	[Fe/H] (dex)
Pr_211.7184+15.5516	211.7184	15.5516	14.885	13.876	15.899	0.017	− 111.27 (2)	0.19	4750	1.31	1.74	− 2.42
Pr_212.5834+10.5365	212.5834	10.5365	14.553	14.082	15.036	0.023	− 125.50 (1)	3.96	6222	4.55	1.09	− 1.79
Pr_213.2814+14.8983	213.2814	14.8983	14.643	14.283	15.006	0.019	− 11.28 (1)	5.46	6002	3.55	1.29	− 1.95†
Pr_213.7878+8.4232	213.7878	08.4232	14.989	14.254	15.573	0.030	− 106.36 (1)	3.40	5289	2.45	1.51	− 2.45*
Pr_214.5557+7.4670	214.5557	07.4670	14.713	14.350	15.106	0.029	+47.24 (1)	5.51	6482	4.10	1.18	− 2.14
Pr_215.6129+15.0163	215.6129	15.0163	14.419	13.688	15.164	0.023	− 120.21 (1)	0.81	5180	2.62	1.40	− 1.92
Pr_215.6783+7.6929	215.6783	07.6929	14.530	13.849	15.019	0.028	+9.50 (1)	0.54	5527	4.00	1.20	− 0.35*
Pr_216.1245+10.2135	216.1245	10.2135	14.683	13.999	15.341	0.027	+106.05 (1)	3.65	5412	2.88	1.30	− 2.21
Pr_217.3862+15.1651	217.3862	15.1651	14.675	14.349	15.125	0.025	− 161.83 (1)	4.11	5700	3.30	1.34	− 1.97
Pr_217.5786+14.0379	217.5786	14.0379	14.765	13.867	15.489	0.029	− 17.17 (3)	0.40	4968	1.64	1.67	− 2.66
Pr_217.6444+15.9634	217.6444	15.9634	14.897	14.562	15.277	0.031	− 19.95 (2)	0.85	6550	4.17	1.17	− 1.82
Pr_218.4256+7.5213	218.4256	07.5213	14.661	13.992	15.322	0.024	+11.45 (2)	0.15	5500	3.80	1.24	− 0.60*
Pr_218.4622+10.3683	218.4622	10.3683	14.998	14.595	15.363	0.023	− 125.40 (2)	1.22	5923	3.50	1.30	− 2.40
Pr_218.4977+15.7251	218.4977	15.7251	14.022	13.144	15.178	0.023	− 32.61 (2)	0.00	5150	4.40	1.12	− 0.16*
Pr_223.5283+11.1353	223.5283	11.1353	14.612	13.537	15.772	0.033	+123.90 (1)	1.31	4540	1.05	1.50	− 2.30
Pr_227.2895+1.3378	227.2895	01.3378	13.917	13.304	14.570	0.051	+4.91 (1)	0.49	5750	4.30	1.14	− 0.35*
Pr_228.4607+8.3553	228.4607	08.3553	14.894	14.587	15.252	0.030	+8.08 (2)	0.01	6525	4.32	1.14	− 2.20
Pr_228.6558+9.0914	228.6558	09.0914	14.832	14.530	15.166	0.032	− 147.32 (2)	0.02	6695	4.26	1.15	− 2.26*
Pr_228.8159+0.2222	228.8159	00.2222	14.751	14.366	15.129	0.052	+5.61 (2)	0.12	6520	4.36	1.13	− 2.02
Pr_229.0409+10.3020	229.0409	10.3020	14.728	13.727	15.790	0.038	− 8.15 (2)	0.21	5400	4.55	1.09	− 0.10
Pr_229.1219+0.9089	229.1219	00.9089	14.747	14.403	15.118	0.048	− 223.25 (2)	0.64	6385	3.70	1.26	− 2.25
Pr_229.8911+0.1106	229.8911	00.1106	14.430	13.577	15.016	0.064	− 2.05 (1)	0.47	5600	4.00	1.20	+0.10*
Pr_230.4663+6.5252	230.4663	06.5252	14.521	13.737	15.098	0.040	− 26.63 (1)	1.09	5348	3.45	1.31	− 1.15*
Pr_231.0318+6.4867	231.0318	06.4867	14.626	13.893	15.183	0.041	+21.45 (1)	0.63	5468	3.90	1.22	− 0.35*
Pr_232.6956+8.3392	232.6956	08.3392	15.076	14.462	15.661	0.044	− 37.84 (2)	0.20	5641	3.40	1.32	− 2.22
Pr_232.8039+6.1178	232.8039	06.1178	15.016	14.268	15.867	0.052	− 212.58 (1)	3.92	5280	2.30	1.54	− 2.26*
Pr_233.5730+6.4702	233.5730	06.4702	14.774	13.869	15.545	0.044	− 80.66 (1)	4.16	4991	1.90	1.62	− 2.74
Pr_233.9312+9.5596	233.9312	09.5596	14.970	14.368	15.557	0.037	− 99.38 (2)	0.29	5505	3.50	1.20	− 2.20
Pr_234.4403+13.3742	234.4403	13.3742	14.817	13.506	15.815	0.046	− 66.48 (2)	0.05	5600	4.51	0.90	− 0.40*
Pr_235.1448+8.7464	235.1448	08.7464	14.649	14.151	15.086	0.042	− 156.26 (1)	4.79	6167	3.64	1.27	− 2.54
Pr_235.7578+9.0000	235.7578	09.0000	14.937	14.601	15.330	0.042	− 58.70 (2)	0.37	6654	4.20	1.16	− 1.81
Pr_235.9710+9.1864	235.9710	09.1864	14.631	14.257	15.069	0.042	− 32.49 (1)	3.69	6300	3.70	1.26	− 1.83*
Pr_236.1077+10.5311	236.1077	10.5311	14.808	13.753	15.809	0.048	− 41.51 (1)	1.79	4650	1.47	1.71	− 2.55
Pr_236.4855+10.6903	236.4855	10.6903	14.575	14.005	14.933	0.052	− 36.42 (1)	0.93	5850	3.70	1.26	− 0.27*
Pr_236.7138+9.6084	236.7138	09.6084	14.529	13.466	15.271	0.045	+54.25 (1)	0.92	5450	3.45	1.31	− 0.85*
Pr_237.8246+10.1427	237.8246	10.1427	15.216	14.501	15.776	0.046	− 165.90 (2)	1.08	5405	2.80	1.44	− 3.23
Pr_237.8353+10.5902	237.8353	10.5902	14.734	13.964	15.370	0.056	− 237.67 (2)	0.31	5250	2.70	1.46	− 2.32*
Pr_237.9609+15.4023	237.9609	15.4023	14.543	14.215	14.916	0.046	− 267.22 (2)	0.66	6557	4.09	1.18	− 1.90
Pr_238.7217+6.1945	238.7217	06.1945	14.770	14.462	15.103	0.039	− 195.14 (2)	0.23	6551	4.20	1.16	− 2.06
Pr_240.0348+13.8279	240.0348	13.8279	14.785	13.835	15.721	0.052	+3.55 (1)	1.80	4760	1.52	1.70	− 2.30
Pr_240.4216+9.6761	240.4216	09.6761	14.944	14.164	15.528	0.040	+37.59 (3)	0.23	5204	2.60	1.47	− 2.98
Pr_241.1186+9.4156	241.1186	09.4156	14.532	14.070	14.999	0.044	− 51.47 (1)	4.89	6299	3.95	1.21	− 1.92
Pr_241.7900+14.0920	241.7900	14.0920	14.680	14.351	15.078	0.038	− 127.80 (2)	0.91	6485	3.90	1.22	− 2.51
Pr_242.3556+7.9425	242.3556	07.9425	14.851	14.461	15.249	0.046	− 181.11 (2)	1.00	6326	3.90	1.22	− 1.95
Pr_243.8390+6.9966	243.8390	06.9966	14.748	14.242	15.192	0.063	− 17.94 (3)	0.32	5878	3.52	1.30	− 1.95
Pr_244.4872+16.8936	244.4872	16.8936	14.379	13.953	14.701	0.043	− 192.08 (2)	0.46	6214	3.90	1.22	− 2.10
Pr_245.1096+8.8947	245.1096	08.8947	14.463	13.739	15.033	0.064	− 30.90 (1)	0.59	5567	4.45	1.11	− 0.35*
Pr_245.4387+8.9954	245.4387	08.9954	14.780	14.354	15.199	0.055	− 82.89 (2)	0.60	6464	4.10	1.18	− 1.67
Pr_245.5747+6.8844	245.5747	06.8844	15.041	14.323	15.579	0.062	− 188.96 (4)	0.79	5424	2.95	1.40	− 3.17
Pr_245.8364+13.8778	245.8364	13.8778	14.012	13.264	14.641	0.045	− 176.99 (1)	4.42	5150	2.28	1.40	− 3.06
Pr_246.8588+12.3193	246.8588	12.3193	14.763	13.932	15.500	0.056	− 86.02 (2)	0.05	5070	2.21	1.50	− 2.25
Pr_248.4394+7.9230	248.4394	07.9230	14.340	13.892	14.767	0.081	− 15.66 (3)	0.85	6350	4.40	1.12	− 1.72
Pr_248.4959+15.0776	248.4959	15.0776	14.717	13.830	15.454	0.062	− 74.03 (2)	0.25	5069	1.86	1.63	− 2.63
Pr_248.5263+8.9342	248.5263	08.9342	15.089	14.279	15.829	0.069	− 109.73 (2)	0.63	5300	2.45	1.51	− 2.07
Pr_250.6971+8.3743	250.6971	08.3743	14.615	13.696	20.337	0.085	− 4.08 (1)	3.84	5020	1.80	1.64	− 2.66
Pr_250.8797+12.1101	250.8797	12.1101	14.261	13.069	15.327	0.053	+4.67 (1)	0.52	5600	4.40	1.12	+0.05*
Pr_251.4082+12.3657	251.4082	12.3657	15.062	14.076	15.785	0.056	− 4.43 (2)	0.03	4919	1.54	1.69	− 3.22
Pr_252.1648+15.0648	252.1648	15.0648	14.621	13.615	15.518	0.068	− 157.06 (1)	2.24	4770	1.35	1.50	− 2.43
Pr_252.4208+12.6477	252.4208	12.6477	14.486	13.739	15.172	0.053	+35.27 (2)	0.05	5500	3.60	1.28	− 1.30*
Pr_252.4917+15.2984	252.4917	15.2984	14.349	13.443	15.056	0.070	+62.65 (1)	0.93	5900	3.70	1.26	− 0.60*
Pr_252.6179+16.0546	252.6179	16.0546	14.178	13.208	15.057	0.074	− 113.39 (2)	0.04	4810	1.60	1.68	− 2.52
Pr_253.8582+15.7240	253.8582	15.7240	14.973	14.037	15.720	0.088	− 98.39 (3)	0.44	5077	2.25	1.50	− 2.58
Pr_254.0662+14.2694	254.0662	14.2694	13.658	13.079	14.172	0.071	− 29.70 (1)	0.46	5500	3.80	1.24	− 0.56*
Pr_254.3844+12.9653	254.3844	12.9653	14.969	13.978	15.743	0.059	− 386.12 (2)	0.47	5300	2.80	1.44	− 2.45†

Table 1 – *continued*

Star	RA (deg)	Dec. (deg)	g_0	i_0	CaHK$_0$	$E(B-V)$	RV (km s^{-1})	σ_{RV}	T_{eff} (K)	log g (cgs)	v_t (km s^{-1})	[Fe/H] (dex)
Pr_254.5215+15.4969	254.5215	15.4969	14.045	13.246	14.807	0.096	+25.01 (1)	0.52	5640	4.30	1.14	− 0.09
Pr_254.5478+10.9129	254.5478	10.9129	14.447	13.687	15.096	0.077	+94.21 (1)	2.72	5460	3.35	1.33	− 2.15
Pr_254.7768+13.8208	254.7768	13.8208	14.018	13.239	14.479	0.077	− 16.41 (1)	0.51	5600	4.05	1.19	− 0.35*
Pr_255.2679+14.9714	255.2679	14.9714	14.332	13.867	14.700	0.083	+27.92 (1)	5.11	6479	3.88	1.22	− 2.09
Pr_255.5564+10.8613	255.5564	10.8613	14.782	14.125	15.306	0.075	− 372.85 (2)	0.43	5495	2.86	1.43	− 2.55
Pr_255.8043+10.8443	255.8043	10.8443	14.246	13.859	14.629	0.082	− 266.01 (2)	1.12	5600	3.20	1.36	− 3.00*

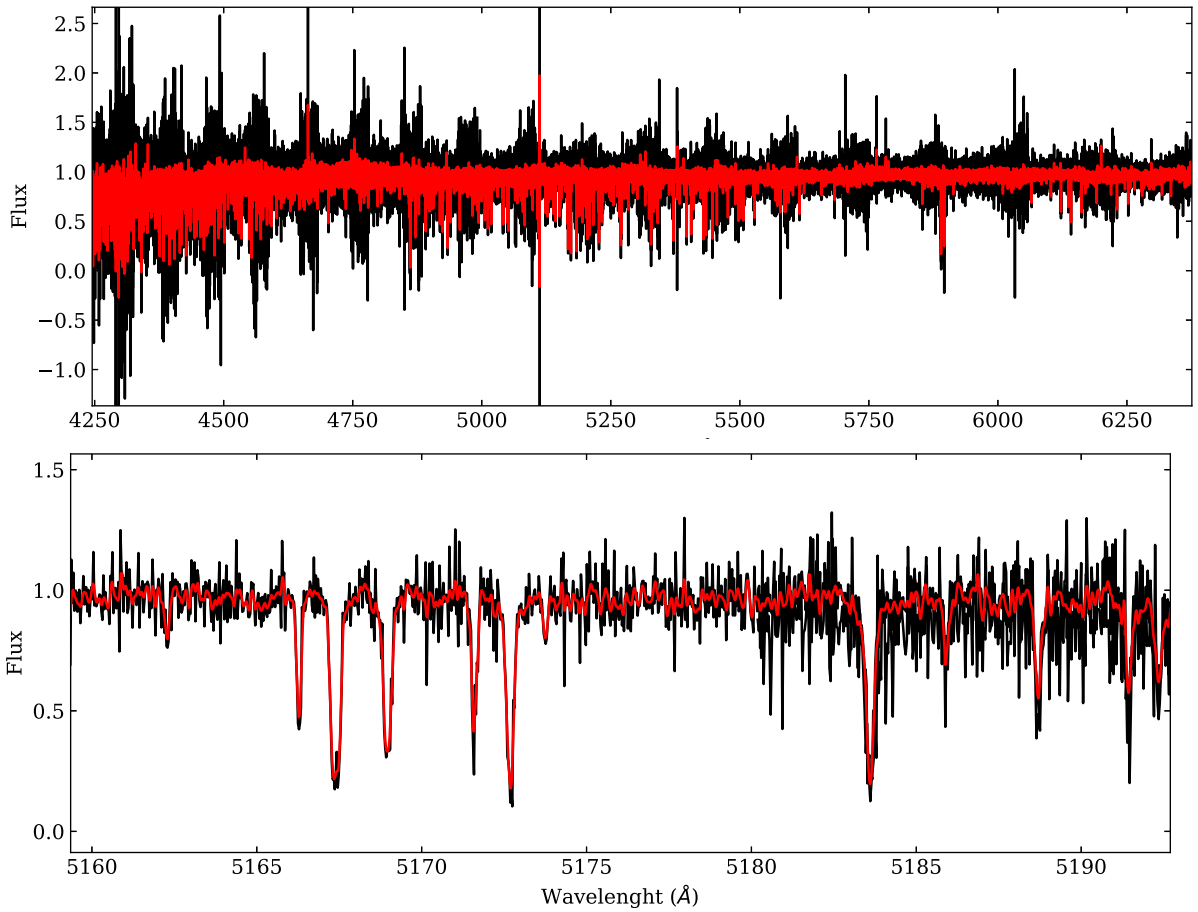

Figure 2. The top panel shows the spectrum of Pr_236.1077+10.5311 in the wavelength range between 4250 and 6300 Å. The bottom panel shows the spectrum of the same star over a limited wavelength range around the magnesium triplet spectral features. The raw ESPaDOnS spectrum from the LIBRE-ESPRIT pipeline is plotted in black. The red line shows the spectrum degraded to a resolution of $R = 40\,000$ and with optimal order merging applied to data (see text).

were excluded as the consequence of the low SNR at the blue end of the spectra.

The stellar atmospheric parameters have been optimized iteratively as follows:

(i) The effective temperatures were derived by minimizing the slopes between iron abundance and excitation potential, allowing the slope to deviate from zero by less than about twice the uncertainty on the slope;

(ii) The surface gravities were obtained from ionization equilibrium between Fe II and Fe I. However, since NLTE impacts the abundances derived from the Fe I lines at low metallicities (e.g. Mashonkina et al. 2017), we tolerated a difference in abundance Δ(Fe II–Fe I) = +0.15 dex for stars with [Fe/H] ≤ -2.5.

(iii) The initial microturbulent velocities were obtained from the empirical relation log g: $v_t = 2.0 - 0.2*\log g$ as in Theler et al. (2020). Convergence to the final value was reached by minimizing the slope between the neutral iron lines and their EWs.

(iv) The model's metallicity was adjusted to the derived Fe I abundance after each iteration until they agreed within ±0.05 dex.

Fig. 3 presents the distribution of our sample in the T_{eff} versus log g diagram. Stars are colour coded according to their metallicity. We consider two sets of isochrones both taken at 13 Gyr and at metallicities [Fe/H] = −3, −2, −1, and 0. The Yonsei–Yale (YY) stellar isochrones (Demarque et al. 2004) (solid lines) assumes an enhancement in α-elements of [α/Fe] = +0.3 at [Fe/H] < −1. The MESA/MIST isochrones are currently only available for solar-scaled

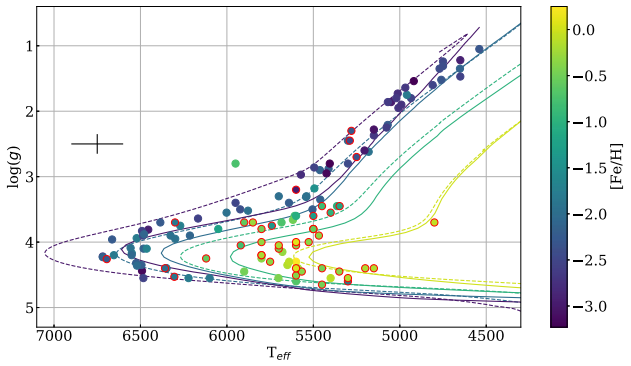

Figure 3. $T_{\rm eff}$ versus log g diagram. Stars are colour coded according to their metallicities. The YY stellar isochrones (solid lines) are shown for the age of 13 Gyr and metallicities [Fe/H] = [−3, −2, −1, 0] from left to right, respectively, with α-enhancement [α/Fe] = +0.3 at [Fe/H] < −1. The MIST/MESA isochrones (dashed lines) with same parameters are also shown, at constant [α/Fe] = 0. Stars denoted with an open red circle have been rejected from the later versions of the *Pristine* catalogues (see text). The black cross indicates the typical uncertainty of 150 K on $T_{\rm eff}$ and 0.15 dex on log g.

abundances (e.g. Choi et al. 2016; Dotter 2016). The YY isochrones seem to better fit our spectroscopic results. Indeed, the TO region of the MIST isochrones is significantly warmer (∼500 K) than the corresponding YY isochrone at [Fe/H] = −3 and none of our sample stars reach this extremely hot temperature. At higher metallicities, the difference between the two sets of models decreases, reaching differences in temperature smaller than $\Delta T_{\rm eff} < 100$ K at [Fe/H] = 0, well within the errors of the spectroscopic $T_{\rm eff}$. As to red giant branch (RGB) stars, the largest difference between the two sets of isochrones is again observed at low metallicities (e.g. $\Delta(T_{\rm eff})_{\rm MIST\text{-}YY} = -100$ K and $\Delta(\log g)_{\rm MIST\text{-}YY} = +0.2$ and at [Fe/H] = –3). However, their difference stays well within the typical spectroscopic uncertainties (150 K in $T_{\rm eff}$ and 0.15 in log g). Thus, both sets of isochrones represent a good fit to data in this region of stellar evolution.

Table 1 lists the final stellar atmospheric parameters adopted in the rest of our analysis. Our sample includes both unevolved and evolved stars with effective temperatures and surface gravities in the interval $T_{\rm eff}$ = 4540–6720 K and log g = 1.05–4.65. It covers a wide range in metallicity, from [Fe/H] = −3.2 to +0.25. As also seen in Fig. 3, all the RGB stars selected by *Pristine* are confirmed VMP stars.

One star stands out from the rest of the sample, Pr_202.3435+13.2291 at $T_{\rm eff}$ = 5950 K, log g = 2.80, and [Fe/H] = −0.75. It is most likely a horizontal branch (HB) star. It was removed from further chemical analysis.

Three stars have very broaden lines, one originates from the new sample and two from the Q6 sample. They are fast rotators (identified with the † symbol in Table 1) and their spectroscopic metallicity is poorly constrained. As a consequence, they were also removed from further chemical analysis. Abundances are provided for a total of 128 stars in Table 2.

3.2 Specific comments on individual abundances

The abundance of carbon was derived by spectral synthesis of the CH absorption at 4300 Å, assuming [O/Fe] = [Mg/Fe] and [N/Fe] = 0 to take into account that some of C can be locked into the CO and CN molecules. While the χ^2 minimization was performed in the 4309-4315 Å window, the continuum was estimated from a wider 60 Å region around the molecular band. The resulting C abundance was finally checked against the 4323 Å absorption band and only concordant band strengths were considered as robust measurements. Fig. 4 provides three examples of our synthesis, corresponding to actual measurements for a cool giant star and a hot dwarf star, and finally the case of an upper limit for a hot star.

The abundance of magnesium was obtained from 2 to 5 Mg I lines at 4571.096 Å, 4702.991 Å, 5172.684 Å, 5183.604 Å, and 5711.088 Å. Spectral synthesis was performed on the strong Mg I lines at 5172.684 Å and 5183.604 Å with EWs larger than 110 mÅ. Fig. 5 illustrates the case of Pr_211.7184+15.5516, for which both strong and weaker lines are available. The results from the four Mg lines are consistent, with a mean [Mg/Fe] = +0.39 and a standard deviation of σ = 0.05.

The abundance of Ca I was obtained from 2 to 20 lines, with EWs between 25 and 100 mÅ. All lines were carefully inspected to retain only the best-fitting ones. This was usually the case in the red part of the spectrum between 5300 and 6700 Å that has a higher SNR.

The abundance of strontium was determined from the single Sr II 4215.519 Å line, since both Sr II 4161.792 Å and 4077.709 Å are too weak and noisy to be measured. Strontium abundances were derived primarily from EW analysis. Additionally, spectral synthesis were performed in case of weak and noisy features. A careful comparison was carried out between results from different methods in order to keep only lines with a good fit or a clear χ^2 convergence.

Barium was measured from 1 to 4 Ba II lines at 4934.076, 5853.668, 6141.713, and 6496.897 Å by spectral synthesis to take into account the HFS of the lines and some small blends with iron lines. The HFS data in the line list are from Prochaska & McWilliam (2000) and Arlandini et al. (1999).

3.3 Uncertainties

(i) Uncertainties due to the atmospheric parameters.
To estimate the sensitivity of the abundances to the adopted atmospheric parameters, we chose three stars representative of three regions in the $T_{\rm eff}$ versus log g diagram (Fig. 3). We repeated the abundance analysis and varied only one stellar atmospheric parameter at a time by its corresponding uncertainty, keeping the others fixed. The estimated internal errors are ±150 K in $T_{\rm eff}$, ±0.15 dex in log (g), and ±0.15 km s^{-1} in $v_{\rm t}$ for cool stars ($T_{\rm eff}$ < 6000 K), and ±200 K in $T_{\rm eff}$, ±0.20 dex in log (g), and ±0.20 km s^{-1} in $v_{\rm t}$ for the warmest stars of the sample ($T_{\rm eff}$ > 6000 K). These errors are presented in Table 3.

(ii) Uncertainties due to EWs measurement. The uncertainties on the individual EW measurements δ_{EWi} are provided by DAOSPEC and computed according to the following formula (Stetson & Pancino 2008):

$$\delta_{EWi} = \sqrt{\sum_p \left(\delta I_p\right)^2 \left(\frac{\partial EW}{\partial I_p}\right)^2 + \sum_p \left(\delta I_{C_p}\right)^2 \left(\frac{\partial EW}{\partial I_{C_p}}\right)^2}, \quad (1)$$

where I_p and δI_p are the intensity of the observed line profile at pixel p and its uncertainty, and I_{C_p} and δI_{C_p} are the intensity and uncertainty of the corresponding continuum. The uncertainties on the intensities are estimated from the scatter of the residuals that remain after subtraction of the fitted line. The corresponding uncertainties σ_{EWi} on individual line abundances are propagated by TURBOSPECTRUM.

The final errors listed in Table 2 were computed following the recipes outlined in Jablonka et al. (2015), Hill et al. (2019), and Lucchesi et al. (2020).

Table 2. Elemental abundances of the 129 stars kept for the chemical analysis. The number of lines used is indicated in parentheses for each element and each star. The quoted errors correspond to the uncertainties resulting from the EW analysis or spectral fitting (see text).

Star	[Fe/H]	log(Fe I) ± σ (N)	log(Fe II) ± σ (N)	[C/Fe] ± σ	[Mg/Fe] ± σ (N)	[Ca/Fe] ± σ (N)	[Sr/Fe] ± σ (N)	[Ba/Fe] ± σ (N)
134.3232	−2.63	4.87 ± 0.04 (17)	4.63 ± 0.09 (3)	+1.17 ± 0.24	+0.19 ± 0.08 (2)	–	+0.03 ± 0.12 (1)	–
180.0090	−0.18	7.32 ± 0.01 (47)	7.30 ± 0.04 (10)	−0.47 ± 0.19	+0.17 ± 0.12 (1)	+0.14 ± 0.08 (2)	–	−0.05 ± 0.09 (4)
180.2206	−2.96	4.54 ± 0.02 (34)	4.58 ± 0.04 (7)	+0.86 ± 0.22	+0.40 ± 0.09 (2)	+0.25 ± 0.09 (2)	<−2.05 (1)	−1.26 ± 0.12 (1)
180.3790	−0.74	6.76 ± 0.02 (95)	6.78 ± 0.02 (16)	+0.02 ± 0.20	+0.22 ± 0.04 (4)	+0.16 ± 0.02 (15)	−0.19 ± 0.08 (1)	+0.05 ± 0.06 (4)
180.7918	−0.08	7.42 ± 0.03 (32)	7.40 ± 0.04 (15)	−0.08 ± 0.20	+0.18 ± 0.12 (1)	−0.05 ± 0.07 (3)	–	+0.18 ± 0.09 (3)
180.9118	−0.49	7.01 ± 0.03 (100)	7.04 ± 0.03 (20)	−0.30 ± 0.25	+0.14 ± 0.06 (3)	+0.11 ± 0.04 (11)	+0.20 ± 0.10 (1)	+0.13 ± 0.06 (4)
181.2243	−2.92	4.58 ± 0.14 (3)	4.37 ± 0.14 (3)	<+2.07	+0.71 ± 0.17 (2)	<+1.00 (4)	–	+0.71 ± 0.24 (1)
181.3119	−1.84	5.66 ± 0.01 (80)	5.67 ± 0.04 (7)	−0.07 ± 0.21	+0.34 ± 0.07 (1)	+0.38 ± 0.02 (15)	−0.19 ± 0.07 (1)	−0.08 ± 0.05 (3)
181.3473	−0.49	7.01 ± 0.01 (94)	7.03 ± 0.02 (18)	+0.25 ± 0.21	+0.11 ± 0.08 (1)	+0.07 ± 0.02 (18)	−0.06 ± 0.08 (1)	+0.08 ± 0.05 (3)
181.4395	−2.50	5.00 ± 0.02 (70)	5.04 ± 0.06 (10)	<−0.12	+0.58 ± 0.07 (4)	+0.35 ± 0.04 (7)	−0.09 ± 0.16 (1)	−0.79 ± 0.06 (3)
181.6954	−0.80	6.70 ± 0.03 (102)	6.75 ± 0.04 (11)	−0.03 ± 0.20	+0.25 ± 0.07 (2)	+0.29 ± 0.03 (14)	–	+0.03 ± 0.05 (4)
182.1670	−0.35	7.15 ± 0.01 (58)	7.20 ± 0.03 (17)	+0.11 ± 0.20	+0.15 ± 0.08 (1)	+0.15 ± 0.03 (9)	+0.24 ± 0.08 (1)	+0.17 ± 0.07 (3)
182.5364	−1.74	5.76 ± 0.03 (53)	5.78 ± 0.04 (10)	<+1.06	+0.24 ± 0.08 (4)	+0.12 ± 0.06 (3)	+0.81 ± 0.10 (1)	+0.07 ± 0.07 (2)
182.8521	−1.79	5.71 ± 0.02 (88)	5.81 ± 0.03 (13)	−0.35 ± 0.20	+0.26 ± 0.06 (4)	+0.20 ± 0.03 (14)	+0.37 ± 0.11 (1)	+0.26 ± 0.07 (3)
183.6850	−3.16	4.34 ± 0.05 (2)	–	<+2.30	+0.01 ± 0.05 (2)	–	–	–
185.4112	−1.85	5.65 ± 0.02 (39)	5.71 ± 0.04 (4)	+0.85 ± 0.22	+0.16 ± 0.06 (2)	+0.42 ± 0.03 (9)	+0.24 ± 0.09 (1)	+0.05 ± 0.12 (2)
187.8517	−0.45	7.05 ± 0.01 (100)	7.13 ± 0.01 (22)	−0.08 ± 0.20	+0.05 ± 0.07 (1)	+0.14 ± 0.02 (13)	−0.19 ± 0.07 (1)	+0.03 ± 0.05 (3)
187.9786	−0.50	7.00 ± 0.01 (73)	6.99 ± 0.03 (15)	−0.02 ± 0.20	+0.30 ± 0.07 (2)	+0.13 ± 0.03 (16)	–	+0.02 ± 0.05 (4)
188.1264	−1.05	6.45 ± 0.02 (112)	6.50 ± 0.04 (15)	+0.24 ± 0.20	+0.18 ± 0.14 (1)	+0.21 ± 0.04 (10)	−0.25 ± 0.14 (1)	−0.46 ± 0.10 (2)
189.9449	−2.57	4.93 ± 0.05 (8)	4.87 ± 0.10 (4)	<+1.44	+0.20 ± 0.14 (1)	+0.46 ± 0.09 (3)	–	<−0.03 (1)
190.2669	−0.34	7.16 ± 0.03 (88)	7.21 ± 0.03 (23)	+0.09 ± 0.20	+0.26 ± 0.10 (1)	+0.08 ± 0.04 (10)	–	+0.28 ± 0.06 (3)
190.5813	−0.20	7.30 ± 0.01 (79)	7.31 ± 0.02 (20)	+0.41 ± 0.20	−0.10 ± 0.06 (3)	+0.12 ± 0.03 (13)	+0.09 ± 0.09 (1)	−0.02 ± 0.05 (4)
190.6313	−0.24	7.26 ± 0.02 (67)	7.30 ± 0.03 (20)	+0.15 ± 0.19	+0.16 ± 0.08 (1)	+0.06 ± 0.03 (12)	–	−0.01 ± 0.05 (3)
192.2121	+0.25	7.75 ± 0.02 (44)	7.71 ± 0.03 (17)	−0.02 ± 0.18	−0.31 ± 0.05 (2)	−0.00 ± 0.03 (6)	−0.80 ± 0.07 (1)	+0.11 ± 0.09 (3)
192.4285	−0.49	7.01 ± 0.01 (65)	7.11 ± 0.03 (15)	+0.32 ± 0.19	+0.09 ± 0.07 (1)	+0.07 ± 0.03 (11)	–	+1.06 ± 0.05 (3)
192.8540	−0.20	7.30 ± 0.01 (82)	7.31 ± 0.01 (22)	+0.10 ± 0.20	−0.01 ± 0.04 (3)	+0.15 ± 0.03 (6)	−0.23 ± 0.07 (1)	+0.12 ± 0.05 (4)
192.9068	−0.35	7.15 ± 0.02 (78)	7.17 ± 0.02 (18)	+0.12 ± 0.20	−0.01 ± 0.05 (3)	+0.13 ± 0.04 (7)	+0.17 ± 0.09 (1)	−0.03 ± 0.07 (4)
193.1159	−1.85	5.65 ± 0.03 (52)	5.60 ± 0.05 (7)	+0.82 ± 0.22	+0.37 ± 0.07 (3)	+0.27 ± 0.07 (4)	+0.35 ± 0.12 (1)	−0.02 ± 0.12 (1)
193.1501	−0.31	7.19 ± 0.01 (91)	7.34 ± 0.03 (20)	−0.03 ± 0.20	−0.08 ± 0.07 (2)	+0.10 ± 0.03 (13)	–	+0.15 ± 0.05 (4)
193.5542	−0.30	7.20 ± 0.01 (72)	7.19 ± 0.02 (18)	−0.04 ± 0.20	+0.03 ± 0.05 (2)	+0.20 ± 0.02 (10)	+0.31 ± 0.07 (1)	+0.12 ± 0.05 (4)
193.8390	−2.91	4.59 ± 0.01 (64)	4.64 ± 0.04 (10)	+0.00 ± 0.25	+0.49 ± 0.06 (3)	+0.25 ± 0.04 (4)	+0.40 ± 0.10 (1)	<−2.00 (1)
196.3755	−2.77	4.73 ± 0.02 (47)	4.74 ± 0.04 (4)	+0.60 ± 0.24	+0.35 ± 0.04 (3)	+0.36 ± 0.04 (3)	–	−0.63 ± 0.05 (3)
196.4126	−0.44	7.06 ± 0.01 (81)	7.01 ± 0.02 (18)	+0.26 ± 0.20	+0.24 ± 0.05 (3)	+0.21 ± 0.03 (11)	−0.15 ± 0.09 (1)	−0.25 ± 0.08 (3)
196.5323	−2.55	4.95 ± 0.04 (24)	4.74 ± 0.14 (3)	–	+0.03 ± 0.10 (3)	+0.27 ± 0.17 (1)	+0.50 ± 0.17 (1)	<−0.04 (1)
196.5453	−2.51	4.99 ± 0.03 (18)	5.08 ± 0.06 (6)	<+0.84	+0.43 ± 0.10 (2)	+0.45 ± 0.06 (5)	+0.41 ± 0.14 (1)	<−0.45 (1)
196.6013	−0.69	6.81 ± 0.01 (76)	6.85 ± 0.03 (10)	+0.16 ± 0.20	+0.34 ± 0.09 (1)	+0.12 ± 0.03 (8)	−0.04 ± 0.09 (1)	+0.06 ± 0.07 (2)
197.5045	−0.80	6.70 ± 0.02 (105)	6.67 ± 0.03 (17)	+0.37 ± 0.21	+0.11 ± 0.07 (2)	+0.22 ± 0.03 (15)	+0.07 ± 0.09 (1)	+0.06 ± 0.06 (4)
197.9861	−1.22	6.28 ± 0.03 (72)	6.30 ± 0.07 (14)	<+0.67	+0.42 ± 0.14 (1)	+0.45 ± 0.06 (7)	–	–
198.5288	−0.59	6.91 ± 0.02 (91)	6.88 ± 0.03 (19)	+0.29 ± 0.23	+0.12 ± 0.05 (3)	+0.00 ± 0.03 (12)	−0.55 ± 0.08 (1)	+0.31 ± 0.05 (3)
198.5495	−2.20	5.30 ± 0.03 (33)	5.23 ± 0.04 (6)	<+1.12	+0.36 ± 0.09 (2)	<+0.24 (4)	+1.06 ± 0.07 (2)	<−0.35 (1)
199.9269	−0.15	7.35 ± 0.01 (56)	7.47 ± 0.02 (19)	+0.11 ± 0.19	−0.01 ± 0.07 (1)	+0.12 ± 0.03 (7)	–	+0.14 ± 0.05 (3)
200.0999	−2.48	5.02 ± 0.04 (57)	5.27 ± 0.07 (8)	<+0.39	+0.26 ± 0.14 (1)	+0.32 ± 0.09 (3)	–	+0.42 ± 0.14 (1)
200.5298	−1.02	6.48 ± 0.03 (98)	6.49 ± 0.03 (12)	−0.05 ± 0.19	+0.42 ± 0.08 (2)	+0.38 ± 0.04 (11)	–	+0.69 ± 0.07 (3)
200.7620	−0.15	7.35 ± 0.02 (63)	7.31 ± 0.03 (15)	+0.14 ± 0.20	−0.04 ± 0.10 (1)	+0.13 ± 0.04 (8)	–	+0.12 ± 0.10 (4)
201.1159	−0.19	7.31 ± 0.02 (63)	7.19 ± 0.02 (18)	−0.01 ± 0.20	+0.06 ± 0.09 (1)	+0.10 ± 0.03 (11)	−0.02 ± 0.09 (1)	−0.04 ± 0.05 (4)
203.2831	−2.70	4.80 ± 0.03 (54)	4.79 ± 0.04 (9)	+0.35 ± 0.23	+0.20 ± 0.08 (4)	+0.28 ± 0.04 (7)	–	−0.65 ± 0.07 (3)
204.9008	−2.66	4.84 ± 0.12 (4)	4.83 ± 0.17 (2)	<+2.25	+0.32 ± 0.14 (3)	–	<−0.49 (1)	–
205.1342	−2.12	5.38 ± 0.03 (66)	5.56 ± 0.05 (6)	−0.01 ± 0.25	+0.17 ± 0.07 (4)	+0.30 ± 0.05 (5)	+0.85 ± 0.12 (1)	+1.30 ± 0.10 (3)
205.8132	−2.13	5.37 ± 0.04 (19)	5.39 ± 0.07 (6)	<+1.43	+0.43 ± 0.11 (2)	–	+1.03 ± 0.15 (1)	<+0.13 (1)
206.3487	−1.80	5.70 ± 0.02 (31)	5.79 ± 0.04 (9)	<+1.17	–	+0.43 ± 0.04 (10)	−0.11 ± 0.10 (1)	−0.38 ± 0.08 (1)
207.9961	−0.49	7.01 ± 0.01 (71)	7.09 ± 0.02 (17)	−0.03 ± 0.19	+0.27 ± 0.08 (1)	+0.22 ± 0.03 (10)	−0.22 ± 0.08 (1)	−0.10 ± 0.05 (4)
208.0799	−2.77	4.73 ± 0.03 (29)	4.80 ± 0.05 (6)	<+0.59	+0.26 ± 0.07 (2)	<+0.39 (5)	–	<−0.10 (1)
209.2123	−1.90	5.60 ± 0.03 (71)	5.56 ± 0.04 (9)	+0.29 ± 0.25	+0.30 ± 0.04 (5)	+0.39 ± 0.04 (8)	+0.69 ± 0.10 (1)	−0.36 ± 0.06 (3)
209.7189	−1.98	5.52 ± 0.03 (22)	5.56 ± 0.06 (5)	<+0.72	+0.06 ± 0.10 (2)	+0.20 ± 0.07 (4)	+0.88 ± 0.14 (1)	<−0.18 (3)
209.9364	−2.25	5.25 ± 0.03 (20)	5.27 ± 0.07 (6)	+2.18 ± 0.23	+0.22 ± 0.07 (3)	+0.37 ± 0.09 (2)	+0.62 ± 0.12 (1)	<+0.91 (2)
210.0175	−2.67	4.83 ± 0.01 (46)	4.95 ± 0.04 (6)	+0.54 ± 0.22	+0.35 ± 0.04 (4)	+0.32 ± 0.03 (7)	+0.21 ± 0.09 (1)	+0.79 ± 0.05 (4)
210.0316	−0.98	6.52 ± 0.01 (93)	6.46 ± 0.01 (16)	−0.08 ± 0.19	+0.38 ± 0.04 (2)	+0.39 ± 0.02 (12)	+0.04 ± 0.07 (1)	−0.20 ± 0.05 (4)
210.7513	−2.12	5.38 ± 0.02 (83)	5.42 ± 0.04 (11)	−0.30 ± 0.22	+0.42 ± 0.04 (4)	+0.35 ± 0.03 (12)	−1.10 ± 0.09 (1)	+0.49 ± 0.05 (4)
210.8633	−1.95	5.55 ± 0.03 (66)	5.57 ± 0.04 (7)	<+0.16	+0.20 ± 0.12 (1)	+0.07 ± 0.06 (4)	+0.46 ± 0.12 (1)	+0.63 ± 0.12 (1)
211.2766	−1.39	6.11 ± 0.02 (88)	6.06 ± 0.03 (11)	+0.08 ± 0.23	+0.64 ± 0.04 (5)	+0.27 ± 0.03 (14)	+0.67 ± 0.10 (1)	+1.12 ± 0.05 (4)
211.7184	−2.42	5.08 ± 0.02 (79)	5.13 ± 0.04 (11)	−0.18 ± 0.23	+0.42 ± 0.04 (4)	+0.29 ± 0.04 (7)	−0.58 ± 0.17 (1)	−0.31 ± 0.05 (4)
212.5834	−1.79	5.71 ± 0.03 (47)	5.65 ± 0.07 (2)	<+0.59	+0.06 ± 0.07 (2)	+0.24 ± 0.04 (8)	+0.22 ± 0.10 (1)	+0.02 ± 0.10 (1)
213.7878	−2.45	5.05 ± 0.03 (54)	5.04 ± 0.04 (9)	+0.73 ± 0.23	+0.71 ± 0.06 (4)	+0.38 ± 0.04 (6)	+0.43 ± 0.10 (1)	−0.69 ± 0.10 (3)
214.5557	−2.14	5.36 ± 0.04 (15)	5.31 ± 0.07 (3)	+2.02 ± 0.30	+0.46 ± 0.07 (2)	–	–	+1.90 ± 0.07 (4)

Table 2 – *continued*

Star	[Fe/H]	log(Fe I) ± σ (N)	log(Fe II) ± σ (N)	[C/Fe] ± σ	[Mg/Fe] ± σ (N)	[Ca/Fe] ± σ (N)	[Sr/Fe] ± σ (N)	[Ba/Fe] ± σ (N)
215.6129	−1.92	5.58 ± 0.01 (86)	5.58 ± 0.03 (11)	+0.15 ± 0.21	+0.33 ± 0.04 (4)	+0.34 ± 0.02 (20)	+0.57 ± 0.09 (1)	−0.05 ± 0.05 (4)
215.6783	−0.35	7.15 ± 0.02 (74)	7.22 ± 0.02 (19)	−0.01 ± 0.20	+0.16 ± 0.07 (2)	+0.10 ± 0.03 (11)	−0.42 ± 0.09 (1)	+0.08 ± 0.05 (3)
216.1245	−2.21	5.29 ± 0.03 (64)	5.24 ± 0.04 (9)	+0.82 ± 0.23	+0.28 ± 0.07 (2)	+0.34 ± 0.07 (2)	–	+0.04 ± 0.06 (3)
217.3862	−1.97	5.53 ± 0.03 (65)	5.58 ± 0.04 (9)	+0.51 ± 0.23	+0.41 ± 0.05 (4)	+0.41 ± 0.03 (11)	+0.19 ± 0.10 (1)	−0.51 ± 0.06 (3)
217.5786	−2.66	4.84 ± 0.01 (57)	4.99 ± 0.04 (9)	+0.02 ± 0.25	+0.47 ± 0.06 (3)	+0.38 ± 0.04 (4)	+1.50 ± 0.09 (1)	+0.35 ± 0.06 (3)
217.6444	−1.82	5.68 ± 0.03 (24)	–	<+1.27	+0.20 ± 0.08 (3)	–	–	+0.63 ± 0.07 (1)
218.4256	−0.60	6.90 ± 0.01 (91)	6.91 ± 0.03 (17)	+0.02 ± 0.19	+0.25 ± 0.07 (2)	+0.41 ± 0.03 (11)	−0.01 ± 0.17 (2)	+0.01 ± 0.06 (3)
218.4622	−2.40	5.10 ± 0.03 (24)	5.15 ± 0.09 (9)	<+0.80	–	+0.39 ± 0.14 (2)	+1.00 ± 0.12 (1)	–
218.4977	−0.16	7.34 ± 0.01 (50)	7.35 ± 0.03 (18)	+0.12 ± 0.19	−0.02 ± 0.07 (1)	+0.05 ± 0.03 (7)	−0.38 ± 0.07 (1)	−0.02 ± 0.09 (3)
223.5283	−2.30	5.20 ± 0.01 (89)	5.32 ± 0.03 (10)	−0.39 ± 0.21	+0.58 ± 0.04 (4)	+0.44 ± 0.03 (10)	+0.74 ± 0.09 (1)	−0.14 ± 0.05 (4)
227.2895	−0.35	7.15 ± 0.02 (92)	7.15 ± 0.02 (23)	+0.13 ± 0.23	+0.20 ± 0.10 (2)	+0.29 ± 0.03 (11)	−0.04 ± 0.09 (1)	+0.21 ± 0.05 (3)
228.4607	−2.20	5.30 ± 0.04 (17)	5.15 ± 0.09 (3)	<+1.30	+0.13 ± 0.09 (3)	–	+0.34 ± 0.14 (1)	<−0.52 (1)
228.6558	−2.26	5.24 ± 0.03 (17)	5.18 ± 0.06 (4)	+1.84 ± 0.25	+0.42 ± 0.12 (1)	+0.28 ± 0.07 (3)	−0.21 ± 0.12 (1)	–
228.8159	−2.02	5.48 ± 0.02 (36)	5.55 ± 0.05 (4)	+1.39 ± 0.25	+0.18 ± 0.04 (4)	+0.37 ± 0.04 (5)	+1.07 ± 0.10 (1)	<−0.29 (1)
229.0409	−0.10	7.40 ± 0.03 (50)	7.47 ± 0.04 (15)	−0.05 ± 0.22	+0.04 ± 0.07 (2)	–	−0.54 ± 0.10 (1)	+0.29 ± 0.06 (3)
229.1219	−2.25	5.25 ± 0.03 (19)	5.26 ± 0.06 (6)	+1.74 ± 0.25	+0.16 ± 0.12 (1)	+0.22 ± 0.07 (3)	+0.92 ± 0.12 (1)	–
229.8911	+0.10	7.60 ± 0.02 (62)	7.59 ± 0.03 (20)	+0.11 ± 0.22	+0.04 ± 0.09 (1)	+0.03 ± 0.03 (10)	–	−0.01 ± 0.05 (3)
230.4663	−1.15	6.35 ± 0.02 (102)	6.35 ± 0.04 (13)	+0.13 ± 0.23	+0.49 ± 0.06 (4)	+0.38 ± 0.03 (12)	+0.45 ± 0.10 (1)	+0.13 ± 0.06 (3)
231.0318	−0.35	7.15 ± 0.02 (69)	7.19 ± 0.03 (22)	−0.16 ± 0.19	+0.10 ± 0.06 (2)	+0.17 ± 0.03 (8)	−0.39 ± 0.09 (1)	−0.06 ± 0.08 (3)
232.6956	−2.22	5.28 ± 0.03 (63)	5.25 ± 0.04 (8)	+0.65 ± 0.23	+0.22 ± 0.06 (3)	+0.26 ± 0.10 (6)	−0.11 ± 0.13 (1)	+0.15 ± 0.07 (2)
232.8039	−2.26	5.24 ± 0.03 (54)	5.21 ± 0.04 (7)	+0.56 ± 0.22	–	+0.15 ± 0.06 (6)	+0.15 ± 0.10 (1)	−1.17 ± 0.07 (2)
233.5730	−2.74	4.76 ± 0.02 (53)	4.76 ± 0.04 (7)	+0.74 ± 0.25	+0.39 ± 0.06 (2)	+0.26 ± 0.04 (5)	+0.31 ± 0.09 (1)	−0.48 ± 0.06 (2)
233.9312	−2.20	5.30 ± 0.02 (50)	5.22 ± 0.03 (7)	+0.53 ± 0.22	+0.33 ± 0.04 (3)	+0.37 ± 0.03 (5)	–	−0.23 ± 0.06 (3)
234.4403	−0.40	7.10 ± 0.02 (72)	7.09 ± 0.04 (10)	+0.25 ± 0.22	+0.33 ± 0.10 (2)	+0.32 ± 0.04 (9)	–	+0.10 ± 0.06 (4)
235.1448	−2.54	4.96 ± 0.04 (22)	4.72 ± 0.05 (4)	<+1.29	+0.55 ± 0.07 (2)	+0.24 ± 0.07 (4)	+0.72 ± 0.10 (1)	+0.01 ± 0.10 (1)
235.7578	−1.81	5.69 ± 0.03 (21)	5.74 ± 0.04 (6)	+1.38 ± 0.25	+0.12 ± 0.07 (4)	+0.32 ± 0.03 (8)	+0.99 ± 0.09 (1)	<−0.42 (2)
235.9710	−1.83	5.67 ± 0.03 (40)	5.67 ± 0.03 (9)	+1.06 ± 0.23	+0.35 ± 0.05 (4)	+0.33 ± 0.04 (6)	+0.56 ± 0.10 (1)	−0.09 ± 0.07 (2)
236.1077	−2.55	4.95 ± 0.01 (77)	4.95 ± 0.04 (9)	−0.22 ± 0.23	+0.42 ± 0.04 (4)	+0.27 ± 0.03 (7)	−0.07 ± 0.10 (1)	+0.09 ± 0.05 (3)
236.4855	−0.27	7.23 ± 0.01 (84)	7.27 ± 0.02 (18)	−0.07 ± 0.22	−0.08 ± 0.05 (3)	+0.07 ± 0.03 (12)	+0.39 ± 0.09 (1)	+0.09 ± 0.07 (3)
236.7138	−0.85	6.65 ± 0.02 (92)	6.70 ± 0.03 (19)	−0.18 ± 0.20	+0.34 ± 0.06 (2)	+0.32 ± 0.02 (14)	–	−0.10 ± 0.10 (3)
237.8246	−3.23	4.27 ± 0.04 (16)	4.16 ± 0.07 (3)	<+0.58	+0.66 ± 0.07 (3)	+0.34 ± 0.07 (3)	+0.05 ± 0.13 (1)	+0.37 ± 0.07 (3)
237.8353	−2.32	5.18 ± 0.02 (58)	5.18 ± 0.04 (8)	+0.35 ± 0.23	+0.35 ± 0.05 (2)	+0.30 ± 0.03 (10)	−0.09 ± 0.12 (1)	−0.07 ± 0.05 (3)
237.9609	−1.90	5.60 ± 0.03 (46)	5.59 ± 0.07 (8)	<+0.76	+0.26 ± 0.07 (3)	+0.26 ± 0.07 (3)	+0.28 ± 0.13 (1)	−0.08 ± 0.13 (1)
238.7217	−2.06	5.44 ± 0.03 (19)	5.15 ± 0.09 (5)	<+0.59	−0.21 ± 0.07 (2)	+0.01 ± 0.10 (1)	–	<−0.32 (1)
240.0348	−2.30	5.20 ± 0.02 (85)	5.27 ± 0.03 (12)	+0.12 ± 0.22	+0.43 ± 0.04 (5)	+0.39 ± 0.03 (6)	+0.46 ± 0.07 (1)	−0.12 ± 0.05 (4)
240.4216	−2.98	4.52 ± 0.02 (27)	4.53 ± 0.05 (5)	+0.74 ± 0.25	+0.27 ± 0.06 (3)	+0.30 ± 0.04 (4)	+0.77 ± 0.08 (1)	+0.84 ± 0.07 (4)
241.1186	−1.92	5.58 ± 0.03 (32)	5.59 ± 0.06 (5)	<+1.14	+0.13 ± 0.12 (1)	+0.24 ± 0.08 (2)	+0.16 ± 0.12 (1)	−0.48 ± 0.12 (1)
241.7900	−2.51	4.99 ± 0.04 (15)	4.65 ± 0.20 (3)	<+2.38	+0.30 ± 0.12 (2)	+0.33 ± 0.07 (6)	+0.12 ± 0.18 (1)	<+0.13 (1)
242.3556	−1.95	5.55 ± 0.03 (22)	5.43 ± 0.07 (5)	<+1.13	+0.01 ± 0.15 (1)	<+0.17 (4)	−0.08 ± 0.15 (1)	<−0.82 (2)
243.8390	−1.95	5.55 ± 0.03 (52)	5.49 ± 0.06 (10)	<+0.15	+0.43 ± 0.09 (3)	+0.39 ± 0.04 (5)	+0.72 ± 0.09 (1)	+0.39 ± 0.09 (1)
244.4872	−2.10	5.40 ± 0.07 (10)	5.34 ± 0.10 (5)	+0.83 ± 0.30	–	–	–	<+0.03 (2)
245.1096	−0.35	7.15 ± 0.01 (69)	7.14 ± 0.03 (15)	−0.02 ± 0.20	+0.06 ± 0.06 (2)	+0.16 ± 0.03 (10)	+0.21 ± 0.07 (1)	−0.06 ± 0.05 (4)
245.4387	−1.67	5.83 ± 0.03 (44)	5.74 ± 0.04 (9)	<+0.94	+0.08 ± 0.12 (3)	+0.26 ± 0.03 (9)	+1.05 ± 0.07 (1)	−0.32 ± 0.07 (2)
245.5747	−3.17	4.33 ± 0.03 (10)	4.17 ± 0.07 (2)	+1.26 ± 0.25	+0.45 ± 0.06 (2)	–	−0.11 ± 0.07 (1)	–
245.8364	−3.06	4.44 ± 0.02 (26)	4.49 ± 0.06 (3)	+0.63 ± 0.23	+0.58 ± 0.05 (4)	+0.44 ± 0.05 (4)	+0.38 ± 0.10 (1)	−0.50 ± 0.07 (2)
246.8588	−2.25	5.25 ± 0.02 (78)	5.27 ± 0.04 (10)	−0.18 ± 0.23	+0.44 ± 0.06 (3)	+0.42 ± 0.04 (6)	+0.13 ± 0.10 (1)	−0.03 ± 0.05 (4)
248.4394	−1.72	5.78 ± 0.01 (51)	5.75 ± 0.04 (8)	+0.61 ± 0.22	+0.23 ± 0.11 (3)	+0.35 ± 0.03 (7)	+0.53 ± 0.06 (1)	+0.11 ± 0.05 (3)
248.4959	−2.63	4.87 ± 0.02 (58)	4.88 ± 0.06 (6)	+0.02 ± 0.25	+0.33 ± 0.05 (3)	+0.30 ± 0.03 (7)	−0.31 ± 0.09 (1)	−0.31 ± 0.05 (3)
248.5263	−2.07	5.43 ± 0.03 (49)	5.36 ± 0.04 (4)	+0.25 ± 0.30	+0.47 ± 0.05 (3)	+0.30 ± 0.04 (4)	+0.24 ± 0.09 (1)	<−0.09 (4)
250.6971	−2.66	4.84 ± 0.03 (58)	4.99 ± 0.04 (8)	<−0.01	+0.36 ± 0.09 (3)	+0.23 ± 0.06 (2)	+0.84 ± 0.09 (1)	−0.25 ± 0.05 (3)
250.8797	+0.05	7.55 ± 0.01 (65)	7.55 ± 0.02 (18)	−0.06 ± 0.20	−0.08 ± 0.06 (2)	+0.05 ± 0.03 (8)	−0.19 ± 0.09 (1)	−0.09 ± 0.05 (3)
251.4082	−3.22	4.28 ± 0.02 (31)	4.20 ± 0.05 (4)	+0.58 ± 0.25	+0.14 ± 0.07 (2)	+0.10 ± 0.10 (1)	<+1.20 (1)	−0.68 ± 0.06 (3)
252.1648	−2.43	5.07 ± 0.01 (69)	5.18 ± 0.05 (3)	−0.06 ± 0.23	+0.31 ± 0.04 (4)	+0.29 ± 0.04 (7)	−0.73 ± 0.09 (1)	−0.72 ± 0.05 (4)
252.4208	−1.30	6.20 ± 0.01 (96)	6.24 ± 0.03 (16)	+0.02 ± 0.22	+0.56 ± 0.06 (4)	+0.35 ± 0.03 (13)	+0.03 ± 0.09 (1)	+0.05 ± 0.05 (4)
252.4917	−0.60	6.90 ± 0.01 (86)	6.99 ± 0.02 (14)	−0.07 ± 0.24	+0.22 ± 0.04 (4)	+0.10 ± 0.02 (14)	+0.17 ± 0.07 (1)	−0.20 ± 0.05 (4)
252.6179	−2.52	4.98 ± 0.01 (72)	5.07 ± 0.03 (8)	+0.34 ± 0.22	+0.57 ± 0.04 (4)	+0.47 ± 0.03 (9)	+0.69 ± 0.07 (1)	−0.09 ± 0.05 (4)
253.8582	−2.58	4.92 ± 0.03 (44)	4.94 ± 0.04 (5)	<+0.55	+0.47 ± 0.06 (3)	+0.17 ± 0.04 (5)	<−1.16 (1)	−0.31 ± 0.06 (3)
254.0662	−0.56	6.94 ± 0.02 (92)	7.01 ± 0.02 (21)	+0.03 ± 0.19	+0.28 ± 0.04 (4)	+0.27 ± 0.02 (13)	−0.02 ± 0.07 (1)	+0.02 ± 0.05 (4)
254.5215	−0.09	7.41 ± 0.01 (66)	7.41 ± 0.01 (19)	+0.07 ± 0.18	−0.07 ± 0.05 (2)	+0.09 ± 0.02 (10)	−0.36 ± 0.07 (1)	+0.12 ± 0.06 (4)
254.5478	−2.15	5.35 ± 0.02 (64)	5.33 ± 0.04 (9)	+0.22 ± 0.21	+0.23 ± 0.04 (4)	+0.26 ± 0.04 (6)	+0.12 ± 0.09 (1)	+0.23 ± 0.05 (4)
254.7768	−0.35	7.15 ± 0.01 (75)	7.12 ± 0.01 (20)	+0.14 ± 0.20	+0.07 ± 0.05 (2)	+0.18 ± 0.02 (11)	−0.09 ± 0.07 (1)	−0.13 ± 0.05 (3)
255.2679	−2.09	5.41 ± 0.03 (33)	5.34 ± 0.07 (7)	<+1.42	+0.11 ± 0.08 (3)	+0.17 ± 0.08 (3)	–	<−0.49 (1)
255.5564	−2.55	4.95 ± 0.03 (33)	5.12 ± 0.06 (4)	+0.56 ± 0.25	+0.61 ± 0.07 (1)	–	+0.50 ± 0.07 (1)	+0.59 ± 0.06 (2)
255.8043	−2.99	4.51 ± 0.05 (9)	4.58 ± 0.09 (3)	+1.23 ± 0.30	+0.63 ± 0.09 (3)	+0.74 ± 0.09 (3)	−0.54 ± 0.14 (1)	<−0.45 (2)

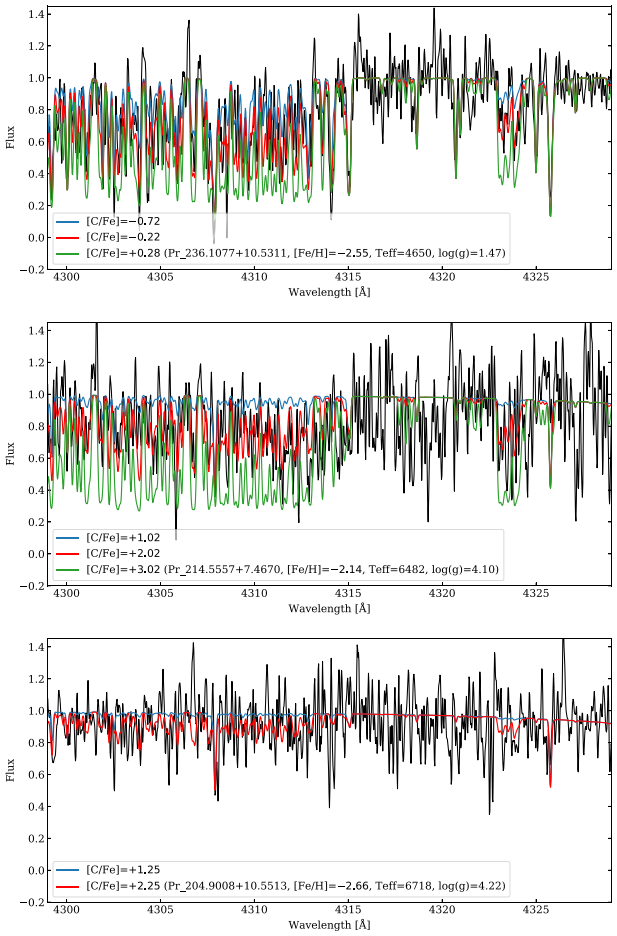

Figure 4. Examples of observed and synthetic spectra in the region of the CH molecular absorption band. *Top panel:* The cool (4650 K) RGB star Pr_236.1077+10.5311 is presented. The red line shows the best synthetic spectrum at [C/Fe] = −0.22. The blue and green lines correspond to the synthetic spectrum when the carbon abundance is decreased and increased by 0.5 dex ([C/Fe] = −0.72 and +0.28), respectively. The difference is clearly seen, especially in the λ4323 Å region, illustrating that the determination of the carbon abundance is robust in cool giants. *Middle panel:* The warm (∼6500 K) TO star Pr_214.5557+7.4670 is presented. At these very high $T_{\rm eff}$, the CH feature is very weak, only high carbon-enhancement can be measured. The red line represents the best synthetic spectrum with [C/Fe] = +2.02, the blue and green colour shows how the CH feature change when the C abundance is decreased and increased by 1.0 dex ([C/Fe] = +1.02 and +3.02), respectively. *Bottom panel:* The warm (∼6700 K) TO star Pr_204.9008+10.5513 is presented. The carbon upper limit is represented by the red synthetic spectrum with [C/Fe] = +2.25. The blue line corresponds to the synthetic spectrum when the carbon abundance is decreased by 1.0 dex ([C/Fe] = +1.25). Both synthetic spectra are at the level of the noise, illustrating that only upper limits at a high [C/Fe] level can be placed for the warmest and most metal-poor stars of the sample.

The dispersion σ_X around the weighted mean abundance of an element X measured from several lines is computed as

$$\sigma_X = \sqrt{\frac{\sum_i (\epsilon_i - \overline{\epsilon})^2}{N_X - 1}}, \quad (2)$$

where N_X represents the number of lines measured for element X, and ϵ stands for the logarithmic abundance.

The final error on the elemental abundances is defined as

$$\sigma_{fin} = \max\left(\frac{\sigma_X}{\sqrt{N_X}}, \frac{\sigma_{Fe}}{\sqrt{N_X}}\right). \quad (3)$$

As a consequence, no element X can have an estimated dispersion $\sigma_X < \sigma_{Fe}$; this is particularly important for species with very few lines.

4 RESULTS

In the following, we compare results from our spectroscopic analysis to literature and discuss the derived elemental abundances in the broader context of evolution of low-mass stars and Galactic chemical evolution.

4.1 Comparison with previous work

To verify the reliability of the derived chemical abundances, we compare our abundance estimates to literature values.

We show in Fig. 6 a comparison between our spectroscopic metallicities and the results derived by Venn et al. (2020) for the stars in common (see Section 2.1). The two investigations agree very well for the 28 stars with [Fe/H] ≤ −2.5 for which Venn et al. (2020) provided full spectroscopic analysis (star symbols in Fig. 6). For these stars, we compute an average difference in metallicity as small as Δ[Fe/H]$_{\rm (Venn\ et\ al.-this\ work)}$ = −0.06 dex (σ = 0.15 dex). Differences in the adopted atmospheric parameters are also small –e.g. $\Delta T_{\rm eff\ (Venn\ et\ al.-this\ work)}$ = 20 K (σ = 40 K) and Δlog g$_{\rm (Venn\ et\ al.-this\ work)}$ = −0.09 dex (σ = 0.17 dex).

For the stars with previous Q6 analysis only (circles in Fig. 6), the agreement is good (Δ[Fe/H]$_{\rm (Venn\ et\ al.-this\ work)}$ = −0.15 dex), however, we also note a significant dispersion (σ = 0.5 dex) towards the metal-rich tail of the [Fe/H] distribution. In this case, part of the observed differences likely results from the adoption of different atmospheric parameters in the two studies. In this work, we derive parameters using the information encoded in the spectra (see Section 3). In contrast, Venn et al. (2020) adopt the 'Bayesian inference method' (Sestito et al. 2019) that makes combined use of SDSS and *Gaia* DR2 photometry, and adopts a priori photometric metallicities from *Pristine* to select the appropriate MESA/MIST isochrone with solar-scaled composition (Paxton et al. 2011; Dotter 2016) to infer parameters. Hence, the assumption of an incorrect metallicity affects the derivation of atmospheric parameters and the estimation of the final [Fe/H]. This is particularly true for stars in the metal-rich regime ([Fe/H] ≥ –1.5) in Fig. 6. For stars with [Fe/H] ≥–1.5, we compute an average difference of $\Delta T_{\rm eff(Venn\ et\ al.-this\ work)}$ = 175 K (σ = 300 K), and Δlog g$_{\rm (Venn\ et\ al.-this\ work)}$ = –0.20 dex (σ = 0.60 dex) that is significantly larger than the one derived for stars with [Fe/H] ≤ –1.5; e.g. $\Delta T_{\rm eff(Venn\ et\ al.-this\ work)}$ = 120 K (σ = 200 K), and Δlog g$_{\rm (Venn\ et\ al.-this\ work)}$ = 0.05 dex (σ = 0.25 dex).

As Venn et al. (2020) adopted the Pristine photometric metallicity estimates a priori, metal-rich stars turn out to be not well calibrated (e.g. $T_{\rm eff}$ and [Fe/H] are degenerate; see section 4.3 in Venn et al. 2020). However, we note that the spectra presented in Venn et al. (2020) were collected between 2016 and 2018 and the *Pristine* metallicity calibrations have improved over the course of these spectroscopic follow-up observations (see discussion in Venn et al. 2020).

Different line list, codes, and minimizing procedures can also play a role. A careful investigation of the observed discrepancy is not the main goal of this study.

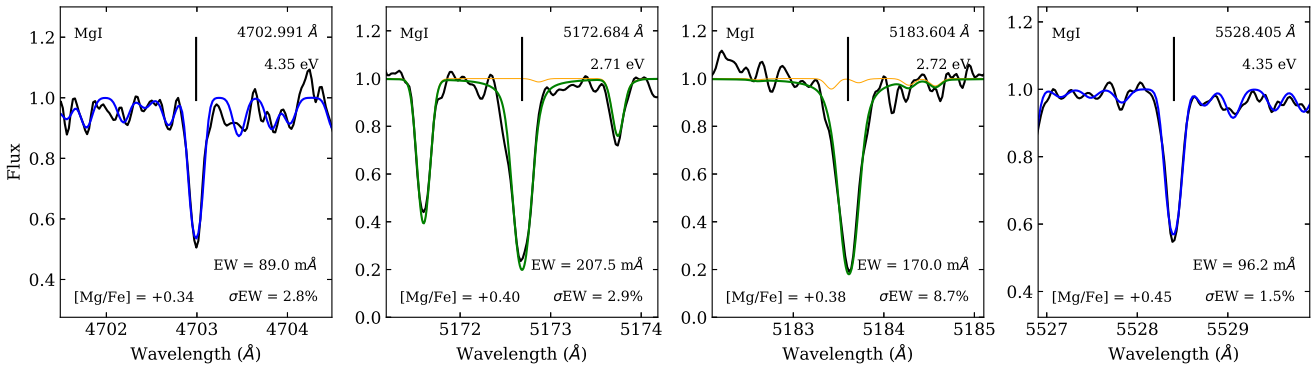

Figure 5. Comparison for star Pr_211.7184+15.5516 of the derived abundances from the four Mg lines available in the spectrum. Abundances from Mg 4702.991 Å and 5528.405 Å were obtained through their EWs (blue colour), abundances of the stronger Mg 5172.684 Å and 5183.604 Å lines were obtained by spectral synthesis (green colour). EW measurements of the latest two are given as indication only and not used for the abundance determination. Abundances are obtained by spectral synthesis, they are very consistent, and they well agree with the EW results with a standard deviation of $\sigma = 0.05$ dex. Orange lines are synthetic spectra without Mg, allowing the identification of blends.

Table 3. Changes in the mean abundances $\delta\log\epsilon(X)$ caused by a change of ±150 K on $T_{\rm eff}$, ± 0.15 on log g, and ± 0.15 on v_t for cool stars (<6000 K) and ±200 K on $T_{\rm eff}$, ± 0.20 on log g, and ± 0.20 on v_t for warm stars (>6000 K), corresponding to the typical uncertainties on the stellar parameters. We provide $T_{\rm eff}$, log g, v_t and [Fe/H] for each of the three representative stars.

El.	$+\Delta T_{\rm eff}$	$-\Delta T_{\rm eff}$	$+\Delta\log g$	$-\Delta\log g$	$+\Delta v_t$	$-\Delta v_t$
			Pr_203-2831+13-6326 (5008 1.95 1.45 − 2.7)			
Fe I	+0.12	−0.15	+0.00	+0.01	−0.02	+0.03
Fe II	+0.01	−0.01	+0.04	−0.06	−0.03	+0.03
C I	+0.35	−0.38	−0.05	+0.05	+0.00	+0.01
Mg I	+0.09	−0.08	+0.00	+0.01	+0.00	+0.01
Ca I	+0.10	−0.12	−0.01	+0.00	−0.02	+0.02
Sr II	+0.21	−0.24	−0.03	+0.03	+0.00	+0.00
Ba II	+0.11	−0.11	+0.05	−0.05	−0.02	+0.02
			Pr_196-6013+15-6768 (5600 4.6 1.08 − 0.69)			
Fe I	+0.06	−0.10	−0.02	+0.01	−0.02	+0.02
Fe II	−0.04	+0.05	+0.05	−0.06	−0.04	+0.04
C I	+0.20	−0.21	−0.03	+0.02	−0.02	+0.02
Mg I	+0.09	−0.09	−0.04	+0.03	−0.01	+0.01
Ca I	+0.10	−0.11	−0.04	+0.03	−0.03	+0.02
Sr II	+0.16	−0.22	−0.05	+0.01	−0.05	+0.01
Ba II	+0.07	−0.07	+0.03	−0.03	−0.04	+0.05
			Pr_206-3487+9-3099 (6522 3.94 1.21 − 1.8)			
Fe I	+0.15	−0.14	−0.02	+0.02	−0.04	+0.06
Fe II	+0.03	−0.03	+0.10	−0.10	−0.10	+0.10
C I	+0.29	−0.28	−0.08	+0.09	+0.00	+0.00
Mg I	+0.13	−0.12	−0.05	+0.04	+0.0	+0.02
Ca I	+0.12	−0.10	−0.03	+0.02	−0.05	+0.03
Sr II	+0.15	−0.14	+0.09	−0.07	−0.17	+0.19
Ba II	+0.14	−0.15	+0.07	−0.09	−0.05	+0.04

4.2 Newly detected very metal-poor stars

We identify 31 new VMP stars in total that were whether missed by the quick analysis in Venn et al. (2020), or are presented in this work for the first time (see Section 2.1).

Among the sample of 20 stars presented in this study for the first time, eight VMP stars (including five stars with [Fe/H] < −2.5 and one EMP star at [Fe/H] = −3, Pr_255.8043+10.8443) have been identified. Interestingly, two of these VMP stars were removed from the more recent versions of the *Pristine* catalogue.

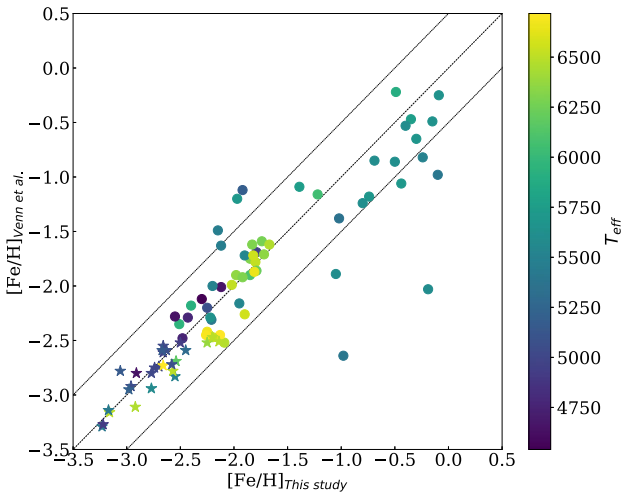

Figure 6. Comparison with the metallicities of Venn et al. (2020) for the 86 stars in common. Colours code the stellar effective temperature. Circles represent the stars whose metallicities were previously only based on the Q6 method of Venn et al. (2020). Star symbols identify stars for which Venn et al. (2020) provided full chemical characterization. For convenience, the one-to-one line and the ±0.5 dex lines are also shown.

Among the 57 stars from Venn et al. (2020) with a Q6 estimation only, no star previously marked at [Fe/H] < −2.5 was missed by the quick analysis. However, an additional set of 19 stars are now identified as VMP, with [Fe/H] < −2.0. From those three have [Fe/H] ∼ −2.5.

Among the 26 stars from Venn et al. (2020) that were rejected by the *Pristine* photometric selection before any analysis, 4 turn out to be actually VMP with −2.5 < [Fe/H] < −2.0.

The six VMP stars ([Fe/H] ≤ = −2) that are erroneously rejected from the more recent version *Pristine* catalogue, are highlighted in red in Fig. 3. Because we are working at the bright end of the catalogue, these stars have saturated flags in one of the *ugri* magnitudes of SDSS. Since *Pristine* aims at maximizing the rejection of contaminants, the later versions of the catalogue conservatively rejects any star that could *potentially* be affected by saturation. In some cases, the *g* and *i* magnitudes that are mainly used to infer the *Pristine* metallicities may in fact not be affected and the inferred

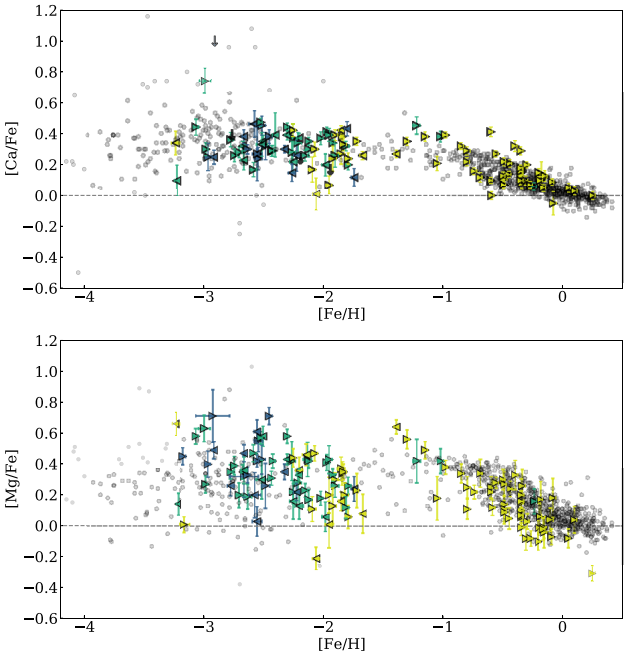

Figure 7. *α-elements:* Calcium (top panel) and magnesium (bottom panel) abundances and upper limits are plotted against metallicity for the full sample. Left and right arrows stand for stars with prograde and retrograde motions, respectively. Yellow, green, and dark blue identify stars in the MW disc, inner halo, outer halo, respectively (see Section 5). Comparison galactic stars (in grey) are from Yong et al. (2013) and Bensby, Feltzing & Oey (2014).

metallicity can be accurate, as shown with some of the rejected stars studied here that we determine to be VMP.

4.3 Abundances for the α-elements: Mg and Ca

In order to gauge the general composition of our sample, Fig. 7 presents the trend of the α-elements, calcium and magnesium, with [Fe/H]. While Mg is produced in hydrostatic H and He nuclear burning in massive core-collapse SNe progenitors, Ca originates mainly from the pre-SN explosion, and can also be produced later by SNela (Woosley & Weaver 1986).

Our sample follows closely the MW halo distribution in Ca and Mg (e.g. Yong et al. 2013). The large majority of the stars in the metal-poor regime ([Fe/H] < -1) are enhanced in α-elements. There is a well-defined plateau at [Ca/Fe] $= +0.3$ dex with a small dispersion of $\sigma \sim 0.1$ dex. We do not find any sub-solar [Ca/Fe] stars in our sample as it had been the case for Caffau et al. (2020). Metal-poor stars are also enhanced in Mg, with a larger dispersion ($\sigma \sim 0.3$ dex) though, arising from the larger uncertainties induced by the smaller number of lines for Mg than for Ca.

Two stars have [Mg/Fe] significantly lower than the rest of our sample at similar [Fe/H]. Pr_192.2121+7.4778 at [Fe/H] $= +0.25$ ($T_{\rm eff} = 5600$K, $\log g = 4.3$) and Pr_238.7217+6.1945 at [Fe/H] $= -2.06$ ($T_{\rm eff} = 6551$, $\log g = 4.2$). The calcium abundance places Pr_238.7217+6.1945 at the low edge of the distribution, at solar [Ca/Fe], as well. Considering that it is among the hottest stars of our sample, very few lines are accessible to the analysis. It looks also depleted in Mg with respect to stars with the same metallicity. However, its [Mg/Fe] abundance ratio is compatible with the main body of the ESPaDOnS sample when errors due to atmospheric parameters (see Table 3) are taken into account.

Pr_192.2121+7.4778 is the most metal-rich star of our sample. At this metallicity, with [Mg/Fe] $= -0.31 \pm 0.05$, it could resemble the Mg-poor MW field stars with globular cluster chemical patterns that Fernández-Trincado et al. (2017) have analysed. However Pr_192.2121+7.4778 is not particularly enriched in Al. Further specific investigation for this star shows that it is not particularly abundant in SNe type Ia products such as Cr or Co either. Moreover [Si/Fe] ~ 0, just as [Ca/Fe], typical of the MW disc stars. Mackereth et al. (2019) have shown from the analysis of APOGEE DR14 the correspondence between the lowest [Mg/Fe] and lowest eccentricity even in the MW disc. At this stage, one can only say that, with $e = 0.175$ this star is indeed in the low quartile of the e-distribution in our sample.

Pr_251.4082+12.3657 at [Fe/H] $= -3.22$ has relatively low α ratios, [Ca/Fe] $= +0.1$ and [Mg/Fe] $= +0.14$, but we do not confirm the sub-solar [Mg/Fe] value found by Venn et al. (2020). However, this star is one of the most metal-poor one of the sample and the single Ca line measurable is weak (< 20 mÅ), making its abundance difficult to ascertain.

At the other end of the abundance ratio distribution, Pr_255.8043+10.8443, at [Fe/H] $= -3$, the EMP from the new sample, is very enriched in both Ca and Mg, at $+0.63$ and $+0.74$, respectively, however, with no other outstanding chemical feature. In particular, only an upper limit to its C abundance could be estimated. As found by Venn et al. (2020), Pr_181.2243+07.4160 has high [Mg/Fe] $= +0.7$ dex and high calcium abundance, however, this is a warm TO star (6450 K) with small Ca features, hence only an upper limit can be placed.

4.4 Carbon abundances and internal mixing

Our sample allows for the investigation of the carbon abundance of MW stars over a wide range of metallicities and to simultaneously explore the impact of internal mixing.

Indeed, during the evolution on the RGB, carbon is converted into nitrogen due to the CN cycle, then mixed to the surface of the star. This mechanisms occurs when low-mass stars (≤ 2.5 M$_\odot$) evolve off the main sequence (MS). Their outer convective envelope starts to move inward, dredging up material that has been processed through the CN-cycle in the inner regions (First Dredge-up, Iben 1964). In a more advanced stage of evolution along the RGB, these stars experience an additional mixing episode just after the RGB bump, when the molecular weight barrier (the μ-barrier) left by the convective envelope at the point of deepest inward progress is canceled out by the outward expansion of the H-burning shell. This extra-mixing episode (Sweigart & Mengel 1979; Charbonnel 1995; Angelou et al. 2012) produces a decline in the surface abundance of carbon ([C/Fe]) and ^{12}C/^{13}C (Briley et al. 1990; Gratton et al. 2000; Martell, Smith & Briley 2008; Gerber, Briley & Smith 2019) and lithium (Lind et al. 2009), and an increase in the nitrogen abundance (Gratton et al. 2000).

The degree of carbon depletion is a function of both metallicity and the initial stellar carbon and nitrogen abundances. This is already discussed extensively in the literature (Spite et al. 2005, 2006; Aoki et al. 2007; Placco et al. 2014; Shetrone et al. 2019). Along this line, Fig. 8 presents the [C/Fe] abundance ratio of our sample stars as a function of their luminosity in three different metallicity bins. The different evolutionary phases, MS and turn-off (TO) stars, lower RGB and upper RGB stars, are identified following the Gratton et al. (2000) classification. In unevolved stars ($\log$ L/L$_\odot$ < 0.8), the average C abundance in stars with [Fe/H] > -1.5 is [C/Fe] $= 0.05 \pm 0.16$ (48 stars). The C abundance appears to increase at first

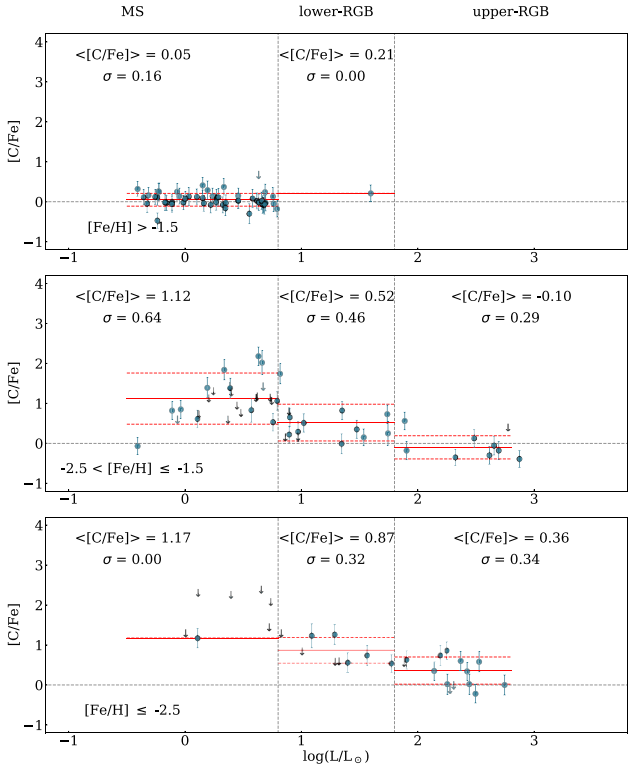

Figure 8. Run of the abundance ratios of [C/Fe] with luminosity for stars with different metallicities (*from top to bottom:* [Fe/H] > -1.5; $-2.5 <$ [Fe/H] ≤ -1.5, and [Fe/H] ≤ -2.5). The dotted vertical lines separate different evolutionary phases – MS and TO stars; lower RGB and upper RGB stars – following the Gratton et al. (2000) classification. The red lines represent the mean carbon abundances along with their standard deviation in the various different evolutionary stages (solid and dashed lines; respectively).

dredge up with a value of [C/Fe] $= 0.21$, however, this apparent increase is only based on a single stars on the lower RGB and thus not significant. In the lower metallicity bins, the carbon depletion is more severe. At the first dredge up, C abundances decrease from [C/Fe] $= +1.12$ to [C/Fe] $= +0.52$ for the stars in the metallicity range $-2.5 <$ [Fe/H] ≤ -1.5, and from [C/Fe] $= +1.17$ to [C/Fe] $= +0.87$ for the lowest metallicity bin [Fe/H] ≤ -2.5.

4.5 Frequency of C-enhanced stars

As discussed by Norris & Yong (2019), the 3D-NLTE treatment of Fe I and CH-based carbon abundances could change our view of the genuine fraction of CEMP stars in the future. Until these calculations are fully accessible, 1D-LTE studies, such as this one, are important.

CEMP stars are commonly separated into two broad categories, according to their chemical composition: carbon enriched stars that display an overabundance of heavy elements formed in slow (s), intermediate (i), or rapid (r) neutron capture processes (CEMP-s, CEMP-i, CEMP-r, and CEMP-r/s); and CEMP-no, stars that display no such excess of neutron-capture elements (Spite et al. 2013). The observed chemical pattern of CEMP-s and CEMP- r/s stars is thought to be the result of mass transfer in a binary system (e.g. Masseron et al. 2010 but see also Hansen et al. 2016).

Our sample encompasses 38 stars with [Fe/H] ≤ -2.0 and measured C abundance (Table 2). 14 of them have [C/Fe] ≥ 0.7 (criterion for CEMP stars of Aoki et al. 2007) and 8 of them have [C/Fe]$\geq$1 (criterion for CEMP stars of Beers & Christlieb 2005).

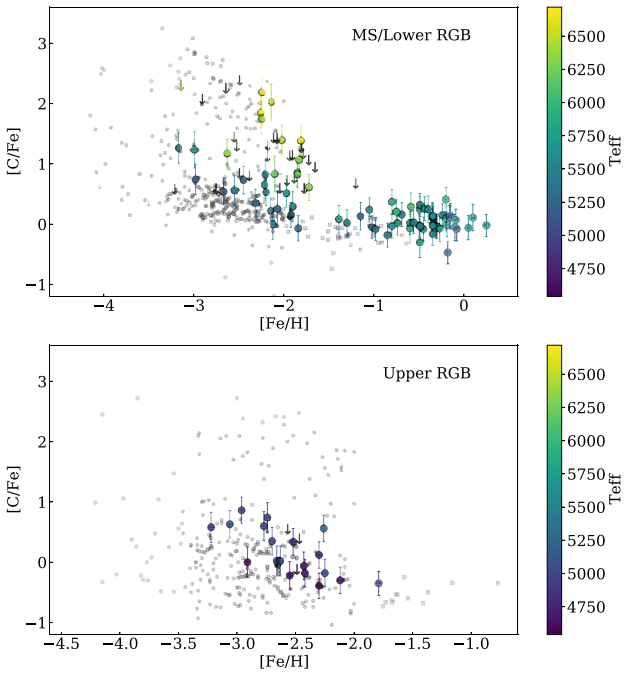

Figure 9. *Top panel:* [C/Fe] abundance ratios are plotted against stellar metallicities [Fe/H] for unevolved stars (e.g. stars with $\log(L/L_\odot) < 1.8$) and colour coded by $T_{\rm eff}$. *Bottom panel:* [C/Fe] abundance ratios are plotted against stellar metallicities [Fe/H] for evolved stars (e.g. stars with $\log(L/L_\odot) > 1.8$). Upper limits for carbon are plotted as downward arrows. The evolutionary phases are based on the work of Gratton et al. (2000). Grey circles are MW halo stars from Placco et al. (2014), whereas grey squares are from Gratton et al. (2000).

This translates into a frequency of CEMP stars of 37 per cent and 21 per cent for the two criteria, respectively. This is consistent with the results of Aguado et al. (2019) that found 41 per cent and 23 per cent, respectively, of CEMP stars in the large medium-resolution survey of *Pristine*. However, we note the number of CEMP stars in Aguado et al. (2019) is likely overestimated due to systematic biases in their derived log g values and a strong dependence of [C/Fe] on log g in their analysis. This issue will be further discussed in Arentsen et al. (in preparation).

Fig. 9 presents the carbon abundances of our ESPaDOnS sample stars depending on their evolutionary stage. The top panel shows the run of [C/Fe] abundance ratios for unevolved stars in the sample ($\log(L/L_\odot) < 1.8$; Gratton et al. 2000), while the bottom panel displays the same trend for the evolved stars ($\log(L/L_\odot) \geq 1.8$) we have analysed.

As summarized in Table 4, the dwarf sub-sample of Placco et al. (2014) has a fraction of 35 per cent and 29 per cent of carbon-rich stars depending on the criterion adopted ([C/Fe] $> +0.7$ versus [C/Fe] $> +1.0$), while our sub-sample of VMP dwarfs is composed of 60 per cent and 40 per cent of C-rich stars considering the same criteria. However, we note that large uncertainties are associated with the derived CEMP fractions (e.g. of the order of $\sim$15 per cent) because of the small size of the observed sample. Also, for warm stars, carbon abundances could be measured only for object with a relatively high level of C overabundance. Both factors must be taken into account when the fractions in Table 4 are compared to literature and larger (an un-biased) samples of EMP stars are required.

The trend with temperature in the dwarf sub-sample is clearly seen in Fig. 9 – the C-rich stars having the highest $T_{\rm eff}$ (>5800 K). This

Table 4. Fraction of CEMP stars in our sample of stars compared to the work of Placco et al. (2014), we consider only the stars with carbon measurements (not the upper limits), and compare the results with the criterion [C/Fe] > +0.7 of Aoki et al. (2007), and [C/Fe] > +1.0 of Beers & Christlieb (2005)

Study	VMP dwarfs	[C/Fe] ≥ +0.7	Fraction	[C/Fe] ≥ +1.0	Fraction
Placco 2014	348 (56 per cent)	123	35 per cent	101	29 per cent
This work	20 (52.5 per cent)	12	60 per cent	8	40 per cent
	VMP giants	[C/Fe] ≥ +0.7	Fraction	[C/Fe] ≥ +1.0	Fraction
Placco 2014	268 (44 per cent)	60	22.4 per cent	48	18 per cent
This work	18 (47.5 per cent)	2	11 per cent	0	0 per cent

correlation is very much driven by the fact that at the low SNR (7–25) in the blue part of the spectra, normal carbon abundances were out of reach for the hot stars. Only the very strong absorption bands of the CEMP stars were measurable (see Fig. 4). In that case, we were facing observational limits rather than a bias in the *Pristine* selection.

The comparison between the upper and lower panels of Fig. 9 illustrates the clear dichotomy between the giants and the dwarfs in our sample. We almost totally lack C-rich giant stars, with only two stars with [C/Fe] > +0.7 (and none with [C/Fe] > +1.0) among our 18 VMP giants, i.e. 11 per cent compared to 22 per cent in the sample of Placco et al. (2014). However, given the small sample size, the errors associated with such fraction is as large as the estimated fraction itself (of the order of ±10 per cent). Thus we cannot draw firm conclusions on the CEMP fraction for evolved giants from such a comparison.

Placco et al. (2014) developed a procedure to compute corrections for the evolutionary depletion of carbon. The corrections tend to increase the C abundances and they depend on the surface gravity, the metallicity of the star, and the observed carbon abundance. The corrections reach up to +0.70 dex at [Fe/H] = −3, log g = 1.0. They would increase the number of giants that can be considered as C-rich in our sample, however, Fig. 9 and Table 4 compare non-corrected abundances only, thus the low CEMP fractions in our subsample of VMP giant is real and probably results from a bias in the *Pristine* photometric selection process of the VMP candidates. This selection appears to favour the warm C-rich TO stars but to be biased against the cooler evolved CEMP stars. Most probably this is also the reason for the very low fraction of C-enhanced stars in Caffau et al. (2020), in which nearly all VMP stars are cool giants. The origin of this *Pristine* selection bias will be further discussed in a forthcoming study (Arentsen et al., in preparation).

4.6 Abundances for the heavy-elements Sr and Ba

Heavy elements (e.g. elements with atomic number greater than 30; Z > Z_{Zn}) are produced through the slow (s) and rapid (r) neutron-capture processes. The main sources of s-process elements are asymptotic giant branch stars (Busso, Gallino & Wasserburg 1999; Bisterzo et al. 2012), while r-process occurs instead in different types of core-collapse SNe (Hillebrandt, Takahashi & Kodama 1976; Woosley et al. 1994; Wanajo et al. 2001; Nishimura et al. 2006; Kratz, Farouqi & Möller 2014) and neutron star merger (Lattimer & Schramm 1974; Freiburghaus, Rosswog & Thielemann 1999; Rosswog et al. 2000; Wanajo 2013; Thielemann et al. 2017).

The wavelength range of the ESPaDOnS spectra includes the spectral features of two neutron-capture elements, Sr and Ba. Because europium is mostly produced by the r-process, [Ba/Eu] ratios are commonly used to identify the origin of the heavy elements. Unfortunately, no Eu lines were measurable in our spectra.

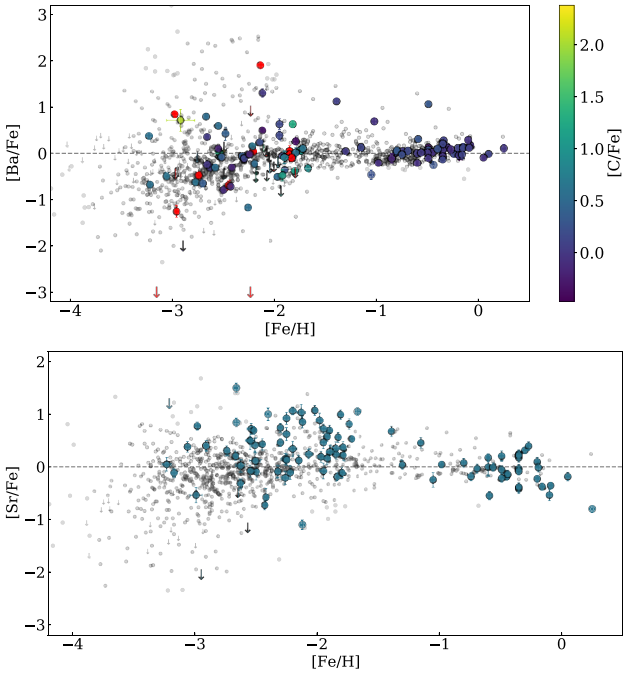

Figure 10. Neutron-capture elements: Barium-to-iron ratio as a function of metallicity at the top, and strontium-to-iron ratio at the bottom. Pointing down arrows are upper limits. Grey dots are galactic comparison stars compiled by Roederer (2013). The [Ba/Fe] ratios are colour coded by their carbon content, red points are carbon-rich stars defined by the criterion of Aoki et al. (2007).

Fig. 10 presents the [Ba/Fe] and [Sr/Fe] measurements of the ESPaDOnS data set compared to MW halo population (Roederer 2013). Barium is generally sub-solar at [Fe/H] < −2 with nevertheless a large scatter with some stars highly enhanced or depleted in barium. Above [Fe/H] ∼ −2, [Ba/Fe] converges to the solar value and the scatter is almost completely removed at [Fe/H] > −1.

The comparison between the C and Ba abundances allows one to identify CEMP-no and CEMP-s stars (Beers & Christlieb 2005). In the absence of Eu, we base our classification on the work of Matsuno et al. (2017), [Ba/Fe] >1 for CEMP-s, adding [Sr/Ba] when possible following Hansen et al. (2019) ([Ba/Fe]>0, [Sr/Ba]<−1.5 for CEMP-r, −1.5 < [Sr/Ba] < −0.5 for CEMP-r/s, and −0.5 < [Sr/Ba] < 0.75 for CEMP-s). While it would not be sufficient to discriminate between CEMP-s and CEMP-r/s (Goswami, Singh Rathour & Goswami 2021), it is probably good enough to distinguish between CEMP-r and the other categories.

We colour code in red in Fig. 10 the stars that are carbon enhanced ([C/Fe] > +0.7). The arrows indicate the CEMP stars for which

only upper limits in Ba could be derived; most of these stars are hot ($T_{\rm eff} > 6200$ K).

A few stars stand out from our sample: Pr_245.5747+6.8844 ([Fe/H] = −3.17) is a CEMP-no star ([C/Fe] = +1.26) without any detectable barium line, while at $T_{\rm eff}$ = 5424K it could be measurable, and its strontium abundance is normal ([Sr/Fe] = −0.1). It is identified in Fig. 10 by its upper limit arbitrarily put at [Ba/Fe] = −3. Again, following the classification of Hansen et al. (2019), Pr_180.2206+9.5683 is another possible CEMP-no star ([Fe/H] = −2.96, [C/Fe] = +0.86) with both low Ba and Sr ([Ba/Fe] = −1.26, [Sr/Fe] < −2.05). Barium was not detectable in two other CEMP stars (Pr_134.3232+17.6970, and Pr_228.6558+9.0914) with [Fe/H] < −2.0. They are all carbon-rich but they are TO stars with effective temperatures ≥ 6350K. At these temperatures the barium spectral features are very weak and require a much higher SNR.

We confirm the finding of Venn et al. (2020) that Pr_214.5557+7.4670 ([Fe/H] = −2.14) is enriched in Ba. This is most probably a CEMP-s candidate with [Ba/Fe] = +1.90 and [C/Fe] = +2.22 (fig. 7 of Matsuno et al. 2017). Unfortunately, its strontium lines are buried in the noise, and the Y lines very much so as well.

The bottom panel of Fig. 10 presents [Sr/Fe] as a function of [Fe/H]. Although our sample is relatively devoid of low abundance ratios, it matches the distribution of the MW stars known so far. One star, Pr_210.7513+12.7744 at [Fe/H] = −2.12, stands out of the general distribution with a significantly lower strontium content level [Sr/Fe] = −1.10 for its metallicity, while its Ba content is normal ([Ba/Fe] = +0.49). This depletion in Sr has essentially been observed in (most of) the ultra-faint dwarfs (UFDs) and is so far understood as the evidence for the second channel of Sr production to be missing in these faint systems, possibly by undersampling of the initial mass function (e.g. Tafelmeyer et al. 2010; Jablonka et al. 2015; Mashonkina et al. 2017; Ji et al. 2019; Sitnova et al. 2021). Interestingly the kinematic analysis of the orbit of Pr_210.7513+12.7744 confirms that it is a halo member, with an orbit almost perpendicular to the plane of the MW (see Section 5), with an apocentre of $R_{\rm apo} = 10.7\ ^{+1.8}_{-1.3}$ kpc.

5 ORBITS

Thanks to *Gaia* EDR3 (Gaia Collaboration 2016, 2021), we can now measure the distances and the orbital parameters of our sample with increased accuracy. The first step for determining the kinematic properties of our stars is to measure their distances. Since it is ill advised to invert the parallax (Bailer-Jones 2015), we infer the distances using a Bayesian inference method. The posterior probability on the distance is composed by two factors, a Gaussian likelihood on the parallax and a prior on the stellar density distribution as in equation (8) from Sestito et al. (2019). We choose a method that does not depend on theoretical isochrones, thereby differing from previous *Pristine* papers (e.g. Sestito et al. 2020; Venn et al. 2020). For the zero-point on the *Gaia* EDR3 parallax, we use the PYTHON code GAIADR3_ZEROPOINT[4] as described in Lindegren et al. (2021). Then, we use GALPY package (Bovy 2015) to determine the orbital parameters. For this analysis, we modify their MWPotential14 assuming a more massive halo of $M = 1.2 \times 10^{12}$ $M_\odot$ compatible with the value from Bland-Hawthorn & Gerhard (2016), as fully described in Sestito et al. (2019, and references therein). We run the orbital inference also for the 112 stars from Venn et al. (2020),

[4]https://gitlab.com/icc-ub/public/gaiadr3_zeropoint

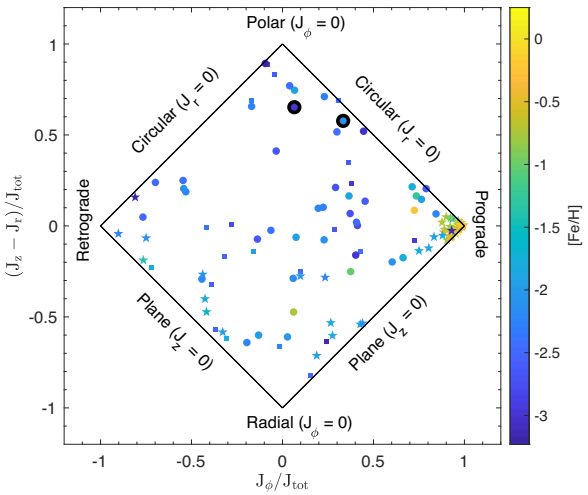

Figure 11. Action plot of the stellar sample colour coded by metallicity. The x-axis is the azimuthal component of the action vector, proxy for rotation. The vertical axis is the difference between the vertical and the radial component of the action vector. Both the axis are normalized by $J_{\rm tot} = J_r + J_z + |J_\phi|$. Squares denote outer halo stars ($R_{apo} \geq 15$ kpc and $Z_{max} > 3.5$ kpc), circles marked the inner halo stars ($R_{apo} < 15$ kpc and $Z_{max} > 3.5$ kpc), while the star symbol denotes the stars confined to the MW plane ($Z_{max} \leq 3.5$ kpc). The two bigger markers with edge colour in black represent Pr_210.7513+12.7744 and Pr_255.8043+10.8443.

since *Gaia* EDR3 provides a better measurement of the astrometric solution than *Gaia* DR2 (Gaia Collaboration 2018), and therefore on the distance and the orbits.

Fig. 11 shows the azimuthal component of the action vector versus the difference between the vertical and the radial components of the action, both axis normalized by the sum of the action components. In this space, stars with different kinematics occupy different portions of this diagram. We divide the total sample of 132 stars into three groups: outer halo ($R_{\rm apo} \geq 15$ kpc and $Z_{\rm max} > 3.5$ kpc), inner halo ($R_{\rm apo} < 15$ kpc and $Z_{\rm max} > 3.5$ kpc), and confined to the disc ($Z_{\rm max} \leq 3.5$ kpc). The limits on the apocentre distance $R_{\rm apo}$ and the maximum height $Z_{\rm max}$ from the MW plane are arbitrarily chosen and follow Sestito et al. (2019, 2020). The chemical distribution of these populations is illustrated in Fig. 7.

This *Pristine*-ESPaDOnS sample is composed of 65 halo stars. The 22 outer halo stars have [Fe/H] ≤ −1.75. The 43 inner halo stars share the same metallicity distribution at the exception of 4 stars, 3 prograde, and 1 $J_\phi = 0$, at [Fe/H] > −1.5 that overlay on the region covers by the MW disc stars. These four stars have a $Z_{\rm max}$ between 3.9 and 7 kpc and the apocentre is between 8 and 9.6 kpc. Two of them have a high eccentricity, 0.77 and 0.9. Their maximum height place them clearly above the plane. They might be born in the disc and then heated up afterwards. In total 67 stars, mostly prograde, are confined in the MW disc. This planar subsample contains 10 high eccentricity stars in the range −2.25 ≤ [Fe/H] ≤ −1.56, 7 of which are prograde, and 4 retrograde. There are also two EMP stars on a disc orbit, one is prograde and the other is retrograde. Finally, all but one planar stars at [Fe/H] ≥ −1.5 are prograde. A full analysis of this sample, in particular regarding the possible association with known stellar structures, is beyond the scope of this paper. However, we focus on two objects, Pr_210.7513+12.7744 and Pr_255.8043+10.8443, whose chemistry stands out from the rest of the sample. The former has a low content of Sr, while the latter is a new EMP star. Both the stars are located in the top region of the action plot in Fig. 11 (see the

larger markers), and they display a prograde polar orbit. This region has been shown to be occupied by the recently discovered LMS-1 stream (Yuan et al. 2020; Malhan et al. 2021), a 60 deg long structure wrapping around the inner region of the MW. The proper motion and position on the sky of Pr_255.8043+10.8443 do not match the ones of LMS-1 (see fig. 4 of Malhan et al. 2021), hence we can exclude a possible association with this stream. As to Pr_210.7513+12.7744, we find differences in RV ($RV \sim 40$ km s^{-1}) and right ascension ($\sim$8 deg) between this star and the best-fitting orbit of LMS-1 (see fig. 4 of Malhan et al. 2021). The comparison of the orbital parameters of Pr_210.7513+12.7744 with the ones of the simulated stars in this stream indicates that an association with the leading trail can be excluded. However, this star might belong to the older wraps of LMS-1, which display a much larger dispersion on their orbital parameters than the leading trail. Would Pr_210.7513+12.7744 be confirmed as a member in the future, it would undoubtedly open new insight into the star formation history of the parent galaxy of LMS-1.

6 SUMMARY AND CONCLUSIONS

We have presented the homogeneous 1D, LTE analysis of 132 stars observed at high resolution with ESPaDOnS, so far the largest sample at high resolution ($R \sim 40\,000$) from the *Pristine* survey. This study expands on the earlier work of Venn et al. (2020), in which only 28 VMP stars were fully chemically characterized. Because this sample is based on the first version of the *Pristine* catalogue, the success rate of identification of genuine EMP stars is not as high as in the later versions. As a consequence, the range of metallicity of our sample extends much beyond -2, reaching [Fe/H] $= +0.25$. Nevertheless, near half of our sample (58 stars) is composed of VMP stars ([Fe/H] ≤ -2). The more metal-rich stars offer us the opportunity of a new and detailed study of the MW halo stellar population. Because it encompasses both dwarf and giant stars, it also enables the analysis of any potential biases induced by the *Pristine* selection process.

Based on *Gaia* EDR3, the orbital analysis of this *Pristine*-ESPaDOnS sample showed that it is composed of 65 halo stars and 67 disc stars. After a general assessment of the sample chemical properties with the α-elements Mg and Ca, we focused on the abundance of carbon and the neutron capture elements, Ba and Sr. Our results can be summarized as follows.

(i) We presented a chemical analysis of 31 newly identified VMP stars, out of which 23 were already presented in Venn et al. (2020) but they were not identified as VMP stars in their Q6 analysis. Eight VMP stars (including five stars with [Fe/H] < -2.5 and one EMP star at [Fe/H] $= -3$) were identified in the subset of 20 stars analysed in this study for the first time.

(ii) Comparing the earliest and latest version of the *Pristine* catalogues, it appears that some VMP stars (six) are missed because their SDSS magnitudes, at the bright end of the selection, are saturated or polluted by instrumental failure. The latest *Pristine* catalogues conservatively reject these objects, even if the *Pristine* metallicity estimate is in fact correct.

(iii) We provide carbon abundances for 97 stars and upper limits for the rest of the sample. From the 38 stars with [Fe/H] ≤ -2.0 and carbon measurements, 14 are CEMP stars following the criterion of Aoki et al. (2007), which sets the C-enrichment threshold at [C/Fe] $= +0.7$. This results in a global frequency of CEMP stars at 37 per cent, which is consistent with other studies.

(iv) However, we almost completely miss the C-rich stars in VMP giants, with only 11 per cent of CEMP stars compared to 22 per cent in the sample of Placco et al. (2014). This is a clear sign for *Pristine* selection bias against carbon-rich giants, which will be analysed in a future work.

(v) Looking at the abundances in Ba, a few VMP stars stand out: Pr_245.5747+6.8844 at [Fe/H] $= -3.17$ is a CEMP-no star. Pr_180.2206+9.5683 at [Fe/H] $= -2.96$ is another CEMP-no candidate. Pr_214.5557+7.4670 ([Fe/H] $= -2.14$) is most probably a CEMP-s star.

(vi) While most our sample is a good match to the known Sr content of the MW population, one star, Pr_210.7513+12.7744 at [Fe/H] $= -2.12$ has a particularly low [Sr/Fe] $= -1.10$ for its metallicity. This is typical of the abundance ratios found in most of the UFDs, making it a possible fossil of accretion in the MW halo. The orbit of Pr_210.7513+12.7744 is perpendicular to the MW plane. Its kinematical parameters are not far from those of the older wraps of LMS-1 stream.

This work clearly shows the enormous potential of the *Pristine* survey and its spectroscopic follow-ups at low and high resolution. Many open issues in modern astrophysics and cosmology can be tackled thanks to the accurate chemical tagging of the EMPs identified by the Pristine photometry and studied with spectroscopy, especially when abundances are combined with the information provided by *Gaia*. For example, large samples of stars with a chemo-dynamical characterization, like the one presented in this paper, can be used to check for possible associations with streams in the halo (e.g. Venn et al. 2020; Kielty et al. 2021). Along the same lines, it would be of interest to obtain high-resolution observations covering larger wavelength ranges (and spectral features of a wider variety of elements) for the two stars that chemo-dynamically stand out from the others (e.g. Pr_210.7513+12.7744 and Pr_255.8043+10.8443; see Section 5) to investigate for possible associations with known structures/accretion events.

Finally, upcoming spectroscopic surveys with high multiplex capabilities – e.g. WAVE (Dalton et al. 2012), 4MOST (de Jong et al. 2019) – will provide us with even larger and more representative samples of metal deficient stars to investigate in fine details the first stages of chemical enrichment of the Galaxy.

ACKNOWLEDGEMENTS

We warmly thank Ian Roederer who very kindly sent us his compilation of Sr and Ba measurements in Milky Way halo stars. This work is based on observations obtained with ESPaDOnS as well as MegaPrime/MegaCam, a joint project of CFHT and CEA/DAPNIA, at the Canada–France–Hawaii Telescope (CFHT) which is operated by the National Research Council (NRC) of Canada, the Institut National des Science de l'Univers of the Centre National de la Recherche Scientifique (CNRS) of France, and the University of Hawaii. The observations at the CFHT were performed with care and respect from the summit of Maunakea which is a significant cultural and historic site. NFM gratefully acknowledge support from the French National Research Agency (ANR) funded project 'Pristine' (ANR-18-CE31-0017) along with funding from INSU,CNRS through the Programme National Galaxies et Cosmologie and through the CNRS grant PICS07708 and from the European Research Council (ERC) under the European Unions Horizon 2020 research and innovation programme (grant agreement No. 834148). The authors thank the International Space Science Institute, Berne, Switzerland for providing financial support and meeting facilities to the international team 'Pristine'. CL acknowledges funding from Ministero dell'Università e della Ricerca through the Programme 'Rita Levi Montalcini' (grant PGR18YRML1). ES acknowledges funding through VIDI grant

'Pushing Galactic Archaeology to its limits' (with project number VI.Vidi.193.093) which is funded by the Dutch Research Council (NWO). KAV is grateful for funding through the National Science and Engineering Research Council Discovery Grants program. This work has made use of data from the European Space Agency (ESA) mission *Gaia* (https://www.cosmos.esa.int/gaia), processed by the *Gaia* Data Processing and Analysis Consortium (DPAC, https://www.cosmos.esa.int/web/gaia/dpac/consortium). Funding for the DPAC has been provided by national institutions, in particular the institutions participating in the *Gaia* Multilateral Agreement.

DATA AVAILABILITY

The data underlying this article will be shared on reasonable request to the corresponding author.

REFERENCES

Aguado D. S. et al., 2019, MNRAS, 490, 2241
Angelou G. C., Stancliffe R. J., Church R. P., Lattanzio J. C., Smith G. H., 2012, ApJ, 749, 128
Aoki W., Beers T. C., Christlieb N., Norris J. E., Ryan S. G., Tsangarides S., 2007, ApJ, 655, 492
Arlandini C., Käppeler F., Wisshak K., Gallino R., Lugaro M., Busso M., Straniero O., 1999, ApJ, 525, 886
Asplund M., Grevesse N., Sauval A. J., Scott P., 2009, ARA&A, 47, 481
Bailer-Jones C. A. L., 2015, PASP, 127, 994
Beers T. C., Christlieb N., 2005, ARA&A, 43, 531
Beers T. C., Preston G. W., Shectman S. A., 1992, AJ, 103, 1987
Bensby T., Feltzing S., Oey M. S., 2014, A&A, 562, A71
Bisterzo S., Gallino R., Straniero O., Cristallo S., Käppeler F., 2012, MNRAS, 422, 849
Bland-Hawthorn J., Gerhard O., 2016, ARA&A, 54, 529
Blanton M. R. et al., 2017, AJ, 154, 28
Bonifacio P. et al., 2019, MNRAS, 487, 3797
Bovy J., 2015, ApJS, 216, 29
Briley M. M., Bell R. A., Hoban S., Dickens R. J., 1990, ApJ, 359, 307
Bromm V., Larson R. B., 2004, ARA&A, 42, 79
Bromm V., Loeb A., 2003, Nature, 425, 812
Busso M., Gallino R., Wasserburg G. J., 1999, ARA&A, 37, 239
Caffau E. et al., 2011, Nature, 477, 67
Caffau E. et al., 2013, A&A, 560, A71
Caffau E. et al., 2017, Astron. Nachr., 338, 686
Caffau E. et al., 2020, MNRAS, 493, 4677
Cayrel R. et al., 2004, A&A, 416, 1117
Charbonnel C., 1995, ApJ, 453, L41
Choi J., Dotter A., Conroy C., Cantiello M., Paxton B., Johnson B. D., 2016, ApJ, 823, 102
Christlieb N., Schörck T., Frebel A., Beers T. C., Wisotzki L., Reimers D., 2008, A&A, 484, 721
Cohen J. G., Christlieb N., Thompson I., McWilliam A., Shectman S., Reimers D., Wisotzki L., Kirby E., 2013, ApJ, 778, 56
Dalton G. et al., 2012, in McLean I. S., Ramsay S. K., Takami H., eds, Proc. SPIE Conf. Ser. Vol. 8446, Ground-based and Airborne Instrumentation for Astronomy IV. SPIE, Bellingham, p. 84460P
de Jong R. S. et al., 2019, Messenger, 175, 3
Demarque P., Woo J.-H., Kim Y.-C., Yi S. K., 2004, ApJS, 155, 667
Deng L.-C. et al., 2012, Res. Astron. Astrophys., 12, 735
Donati J. F., Catala C., Landstreet J. D., Petit P., 2006, in Casini R., Lites B. W., eds, ASP Conf. Ser. Vol. 358, Solar Polarization 4. Astron. Soc. Pac., San Francisco, p. 362
Dotter A., 2016, ApJS, 222, 8
Eisenstein D. J. et al., 2011, AJ, 142, 72
Fernández-Trincado J. G. et al., 2017, ApJ, 846, L2
Frebel A., 2018, Annu. Rev. Nucl. Part. Sci., 68, 237
Frebel A., Norris J. E., 2015, ARA&A, 53, 631
Freiburghaus C., Rosswog S., Thielemann F. K., 1999, ApJ, 525, L121
Gaia Collaboration, 2016, A&A, 595, A1
Gaia Collaboration, 2018, A&A, 616, A1
Gaia Collaboration, 2021, A&A, 649, A1
Gerber J. M., Briley M. M., Smith G. H., 2019, AJ, 157, 154
Goswami P. P., Singh Rathour R., Goswami A., 2021, A&A, 649, A49
Gratton R. G., Sneden C., Carretta E., Bragaglia A., 2000, A&A, 354, 169
Hansen T. T., Andersen J., Nordström B., Beers T. C., Placco V. M., Yoon J., Buchhave L. A., 2016, A&A, 588, A3
Hansen C. J., Hansen T. T., Koch A., Beers T. C., Nordström B., Placco V. M., Andersen J., 2019, A&A, 623, A128
Heger A., Woosley S. E., 2010, ApJ, 724, 341
Hill V. et al., 2019, A&A, 626, A15
Hillebrandt W., Takahashi K., Kodama T., 1976, A&A, 52, 63
Iben I. Jr., 1964, ApJ, 140, 1631
Ivans I. I., Sneden C., James C. R., Preston G. W., Fulbright J. P., Höflich P. A., Carney B. W., Wheeler J. C., 2003, ApJ, 592, 906
Jablonka P. et al., 2015, A&A, 583, A67
Jacobson H. R. et al., 2015, ApJ, 807, 171
Ji A. P., Simon J. D., Frebel A., Venn K. A., Hansen T. T., 2019, ApJ, 870, 83
Keller S. C. et al., 2007, Publ. Astron. Soc. Aust., 24, 1
Khoperskov S., Haywood M., Snaith O., Di Matteo P., Lehnert M., Vasiliev E., Naroenkov S., Berczik P., 2021, MNRAS, 501, 5176
Kielty C. L. et al., 2021, MNRAS, 506, 1438
Kratz K.-L., Farouqi K., Möller P., 2014, ApJ, 792, 6
Kupka F. G., Ryabchikova T. A., Piskunov N. E., Stempels H. C., Weiss W. W., 2000, Balt. Astron., 9, 590
Lattimer J. M., Schramm D. N., 1974, ApJ, 192, L145
Lind K., Primas F., Charbonnel C., Grundahl F., Asplund M., 2009, A&A, 503, 545
Lindegren L. et al., 2021, A&A, 649, A4
Lucchesi R. et al., 2020, A&A, 644, A75
Mackereth J. T. et al., 2019, MNRAS, 482, 3426
Majewski S. R., APOGEE Team, APOGEE-2 Team, 2016, Astron. Nachr., 337, 863
Malhan K., Yuan Z., Ibata R., Arentsen A., Bellazzini M., Martin N. F., 2021, ApJ, 920, 51
Martell S. L., Smith G. H., Briley M. M., 2008, PASP, 120, 7
Mashonkina L., Jablonka P., Sitnova T., Pakhomov Y., North P., 2017, A&A, 608, A89
Masseron T., Johnson J. A., Plez B., van Eck S., Primas F., Goriely S., Jorissen A., 2010, A&A, 509, A93
Matsuno T., Aoki W., Suda T., Li H., 2017, PASJ, 69, 24
Mucciarelli A., 2013, preprint (arXiv:1311.1403)
Nishimura S., Kotake K., Hashimoto M.-a., Yamada S., Nishimura N., Fujimoto S., Sato K., 2006, ApJ, 642, 410
Nissen P. E., Schuster W. J., 2010, A&A, 511, L10
Norris J. E., Yong D., 2019, ApJ, 879, 37
Pagel B. E. J., Cambridge Univ. Press Cambridge 1997, Nucleosynthesis and Chemical Evolution of Galaxies
Paxton B., Bildsten L., Dotter A., Herwig F., Lesaffre P., Timmes F., 2011, ApJS, 192, 3
Piskunov N. E., Kupka F., Ryabchikova T. A., Weiss W. W., Jeffery C. S., 1995, A&AS, 112, 525
Placco V. M., Frebel A., Beers T. C., Stancliffe R. J., 2014, ApJ, 797, 21
Plez B., 2012, Astrophysics Source Code Library, record ascl:1205.004
Prochaska J. X., McWilliam A., 2000, ApJ, 537, L57
Roederer I. U., 2013, AJ, 145, 26
Roederer I. U., Preston G. W., Thompson I. B., Shectman S. A., Sneden C., Burley G. S., Kelson D. D., 2014, AJ, 147, 136
Rosswog S., Davies M. B., Thielemann F. K., Piran T., 2000, A&A, 360, 171
Ryabchikova T. A., Piskunov N. E., Kupka F., Weiss W. W., 1997, Balt. Astron., 6, 244
Sakari C. M. et al., 2019, ApJ, 874, 148
Schlegel D. J., Finkbeiner D. P., Davis M., 1998, ApJ, 500, 525
Sestito F. et al., 2019, MNRAS, 484, 2166
Sestito F. et al., 2020, MNRAS, 497, L7
Shetrone M. et al., 2019, ApJ, 872, 137

Sitnova T. M. et al., 2021, MNRAS, 504, 1183
Spite M. et al., 2005, A&A, 430, 655
Spite M. et al., 2006, A&A, 455, 291
Spite M., Caffau E., Bonifacio P., Spite F., Ludwig H. G., Plez B., Christlieb N., 2013, A&A, 552, A107
Starkenburg E. et al., 2017, MNRAS, 471, 2587
Starkenburg E. et al., 2018, MNRAS, 481, 3838
Steinmetz M. et al., 2006, AJ, 132, 1645
Stetson P. B., Pancino E., 2008, PASP, 120, 1332
Sweigart A. V., Mengel J. G., 1979, ApJ, 229, 624
Tafelmeyer M. et al., 2010, A&A, 524, A58
Theler R. et al., 2020, A&A, 642, A176
Thielemann F. K., Eichler M., Panov I. V., Wehmeyer B., 2017, Annu. Rev. Nucl. Part. Sci., 67, 253
Van der Swaelmen M., Hill V., Primas F., Cole A. A., 2013, A&A, 560, A44
Venn K. A. et al., 2020, MNRAS, 492, 3241
Wanajo S., 2013, ApJ, 770, L22
Wanajo S., Kajino T., Mathews G. J., Otsuki K., 2001, ApJ, 554, 578
Woosley S. E., Weaver T. A., 1986, ARA&A, 24, 205
Woosley S. E., Wilson J. R., Mathews G. J., Hoffman R. D., Meyer B. S., 1994, ApJ, 433, 229
Xing Q.-F., Zhao G., Aoki W., Honda S., Li H.-N., Ishigaki M. N., Matsuno T., 2019, Nat. Astron., 3, 631
Yanny B. et al., 2009, AJ, 137, 4377
Yong D. et al., 2013, ApJ, 762, 26
York D. G. et al., 2000, AJ, 120, 1579
Youakim K. et al., 2017, MNRAS, 472, 2963
Yuan Z., Chang J., Beers T. C., Huang Y., 2020, ApJ, 898, L37

This paper has been typeset from a TEX/LATEX file prepared by the author.